

LA-UR-21-31464

Approved for public release; distribution is unlimited.

Title: Sea ice evolution along the Northern Sea Route and implications for trans-Arctic shipping from 2021 through 2060

Author(s): D'Angelo, Gennaro
Hunke, Elizabeth Clare
Pitts, Travis Ray
Price, Stephen F. Dr
Roberts, Andrew Frank

Intended for: Report

Issued: 2021-11-18

Disclaimer:

Los Alamos National Laboratory, an affirmative action/equal opportunity employer, is operated by Triad National Security, LLC for the National Nuclear Security Administration of U.S. Department of Energy under contract 89233218CNA000001. By approving this article, the publisher recognizes that the U.S. Government retains nonexclusive, royalty-free license to publish or reproduce the published form of this contribution, or to allow others to do so, for U.S. Government purposes. Los Alamos National Laboratory requests that the publisher identify this article as work performed under the auspices of the U.S. Department of Energy. Los Alamos National Laboratory strongly supports academic freedom and a researcher's right to publish; as an institution, however, the Laboratory does not endorse the viewpoint of a publication or guarantee its technical correctness.

Sea ice evolution along the Northern Sea Route and implications for trans-Arctic shipping from 2021 through 2060

Gennaro D'Angelo, Elizabeth Hunke, Travis Pitts, Stephen Price, Andrew Roberts
Los Alamos National Laboratory

November 15, 2021

1 Executive Summary

- Arctic surface temperatures warmed at twice the global average in the second half of the 20th century due to Arctic amplification (AA), a phenomenon predominantly caused by regional polar changes, like the melting of perennial sea ice and reduced sea ice extent (leading to more solar radiation being absorbed by the ocean surface as opposed to being reflected back to space by the ice surface). AA is projected to reach a factor of three even if the climate is stabilized by the mid 21st century by reduced greenhouse gas emissions. In all emissions scenarios, AA is projected to lead to temperature changes at least 2.4 times larger than global mean surface temperature changes occurring between 2070 and 2100 (see Q1, Section 3.1).
- The ice-albedo feedback, which occurs when the polar-marine surface absorbs more radiation as highly reflective sea ice melts, is reversible such that the premise of a runaway process is no longer accepted as a realistic possibility (see Q2, Section 3.1).
- No matter what actions are taken to reduce CO₂ concentrations in the atmosphere from now on, two different methods of predicting an ice-free Arctic suggest that perennial sea ice will mostly disappear in September by the year 2050. If there is no reduction in anthropogenic CO₂ and methane emissions, that scenario could occur sooner than 2030 (see Q3, Section 3.1).
- Defining Arctic navigability as safe and economic passage of Polar Class 7 (see IMO, *International Maritime Organization*, 2002) cargo ships without need of an escorting icebreaker, no single trans-Arctic ship route will be navigable year-round in the first half of the 21st century, including in the strong emission scenarios. However, seasonal trans-Arctic navigability will increase this century (see Q4, Section 3.1).
- An estimate on the number of days per year that the Northern Sea Route (NSR) will be navigable in the future is beyond the scope of this report (see Q1, Section 3.2).
- Along Northern Sea Routes 5 and 6 (see Figure 2), which run close to the Russian coast and Yamal LNG plant, an ARC 7 ice class LNG tanker, the equivalent of a Polar Class 3 (PC3) vessel, will be at low risk in December through April at some point during the current decade. May will continue to entail some risk (more than April) along relatively short segments of these routes through the end of the next decade (2030-2039). Come June, snow rapidly melts away, and thereafter the underlying sea ice begins becomes thinner and less concentrated, greatly reducing risk (see Q2, Section 3.2). However, neither path is desirable for ARC 7 tankers due to shallow bathymetry in Sannikov Strait, and a more desirable path for these ships passes to the north of the New Siberian Islands (route 20, discussed further below).

- Conventional LNG tankers (i.e., non-ice-strengthened vessels according to the IMO classification), without icebreaker escorts, will continue to encounter dangerous or impassable conditions along many sections of the NSR through the end of this decade for many months of the year. Through 2039, these conventional tankers will be able to operate safely along NSR 6 (see Figure 2) from August through October. By 2040-2049, the span of safe operation increases to August through November, and by 2050-2059 it increases to July through November, assuming a northward deviation to avoid the Sannikov Strait (see Q3, Section 3.2).
- Different sections of the NSR will experience different levels of risk at different times of year and depending on the vessel ice class. Refer to Section 4.6 for details (see Q4, Section 3.2).
- Assuming an ARC 7 vessel traveling from the Yamal Peninsula region along NSR 6 in May of the current decade (2020-2029), a minimum estimate for the total travel time to the Bearing Strait would be 2105 NM / 19.5 knots (ice free conditions) + 325 NM / 5 knots (non-ice free conditions) = 173 hours = 7.2 days. Under the same assumptions but in June (or alternatively, even in May by 2040-2049), minimum travel time along the entire ice free route would be 2105 NM / 19.5 knots = 125 hrs = 5.2 days (see Q5, Section 3.2).

2 Introduction

This report provides answers to key questions about changes in Arctic climate and Arctic sea ice conditions as a function of climate change over the next four decades (2020-2029, 2030-2039, 2040-2049, 2050-2059), with a focus on impacts to Arctic shipping routes. Answers to general questions covering the entire Arctic region are addressed first, based on our best understanding of the most recent literature on this topic. For answers to more specific questions about changes in conditions along the Northern Sea Route (NSR), which is part of a cluster of possible East Arctic Routes, we turn to a detailed, multi-model ensemble analysis that takes advantage of the most recent set of climate model outputs available from CMIP6 (*Tebaldi et al.*, 2021a).

3 Response to key questions

3.1 Arctic sea ice in a changing climate

This Section includes answers to questions regarding broad-scale changes in the Arctic, and in particular sea ice, in response to a changing climate.

1) How much greater is the Arctic warming compared to the rest of the world average? Two or three times the average, or a different number? And is that projected to change?

Arctic surface temperatures north of 60°N warmed at twice the global average in the second half of the 20th century (*Johannessen et al.*, 2004), a phenomenon known as Arctic amplification (AA). Amplification has continued into the 21st century, and is predominantly caused by regional polar changes including melting of perennial sea ice and reduced sea ice extent, rather than advection of heat from lower latitudes (*Stuecker et al.*, 2018; *Dai et al.*, 2019). The AA signal is strongest in winter, but because it is closely related to changes in sea ice (*Davy et al.*, 2018), there may come a time when perennial Arctic sea ice loss in summer reduces the annually-averaged AA below current levels (e.g. *Muntjewerf et al.*, 2020). However, based on the most recent analysis of multi-model ensembles from Phase 6 of the Coupled Model Intercomparison Project (CMIP6; *Eyring et al.*, 2016), AA is projected to reach a factor of three even if climate is stabilized by the mid 21st century due to much reduced greenhouse gas emissions, and in all emissions scenarios AA

is projected to be at least 2.4 times larger than global surface temperature changes within the 2070-2100 analysis window (*Davy and Outten, 2020*).

2) When might a runaway Arctic ice albedo feedback occur and how likely is it to occur?

The sea ice albedo feedback occurs when the polar marine surface absorbs more radiation as highly reflective sea ice melts to reveal the ocean upon which it floats. In fact, the ocean *absorbs* up to $\approx 96\%$ of incident solar radiation as compared to sea ice with surface snow *reflecting* as much as $\approx 85\%$, so that as the open water fraction increases, warming of the ice-ocean boundary layer accelerates, melting more sea ice below the water line, resulting in a positive feedback. This feedback, which operates equally well in reverse (i.e., as it gets cooler, more ice forms, which reflects more radiation with the potential to increase cooling or at least decrease warming), has been widely observed and modeled (e.g. *Perovich et al., 2008; Steele et al., 2010*). Previous one dimensional numerical experiments had even suggested that reversing its impact on the climatic loss of perennial sea ice may face non-linear thresholds before sea ice could grow again in a cooling climate (*Eisenman and Wettlaufer, 2009*). However, experiments utilizing the full state space of the Community Earth System Model (CESM) indicate that no such irreversibility exists (*Armour et al., 2011*), and the premise of a runaway process is now consigned to history.

3) When is the Arctic projected to face an ice-free summer?

No matter what actions are taken to reduce CO₂ concentration in the atmosphere from now on, two different methods of predicting an ice free Arctic suggest that perennial sea ice will mostly disappear in September by the year 2050. If there is no reduction in anthropogenic CO₂ and methane emissions, that scenario could occur sooner than 2030.

An ice-free Arctic is commonly defined as less than 1 million km² of ocean masked by at least 15% sea ice coverage in the northern hemisphere (*Jahn and Holland, 2013*). We draw on three recent papers that predict this scenario in the 21st century, and found none published in the last decade that didn't. The first paper uses a simple correlation between global atmospheric CO₂ concentration and sea ice extent (*Notz and Stroeve, 2016*). The second and third provide comprehensive analysis of fully coupled earth system model contributions to Phase 6 of the the Coupled Model Intercomparison Project (CMIP6; *Notz and Community, 2020; Davy and Outten, 2020*). We focus on two projections from these studies for climate change mitigation scenarios RCP-4.5 and RCP-8.5 for the correlative study, and roughly equivalent Shared Socioeconomic Pathway SSP2 and SSP5 for the CMIP6 analysis. These scenarios correspond to "middle of the road" climate change mitigation efforts (RCP-4.5, SSP2) and persistent fossil-fueled development (RCP-8.5, SSP5, see *Riahi et al., 2017*). For these, the simple statistical relationship of *Notz and Stroeve (2016)* predicts that by 2050, the Arctic will be ice-free during August and September for middle-of-the-road mitigation and from July to November for a fossil-fueled future. The CMIP6 ensemble predicts that the Arctic will be ice free in September by 2050 for both scenarios, with multi-decadal spread between viable models (*Notz and Community, 2020*). Even under strict climate change mitigation policy, the CMIP6 models suggests the Arctic will be ice-free in September before 2050, but could stabilize by 2060 in strong emission reduction scenarios not part of SSP2 or SSP5 (*Davy and Outten, 2020*). This is consistent with the simpler *Notz and Stroeve (2016)* model, that even reaches an ice free September by 2050 under a more aggressive emission reduction scenario. For the SSP2 and SSP5 cases in CMIP models, an ice free Arctic in September will likely come much sooner, with some models predicting near-collapse of the perennial ice cover this decade.

4) When are the various Arctic routes (Northwest Passage, Northeast Route, Northern Sea Route, Transpolar Route, etc) expected to have year-round navigability?

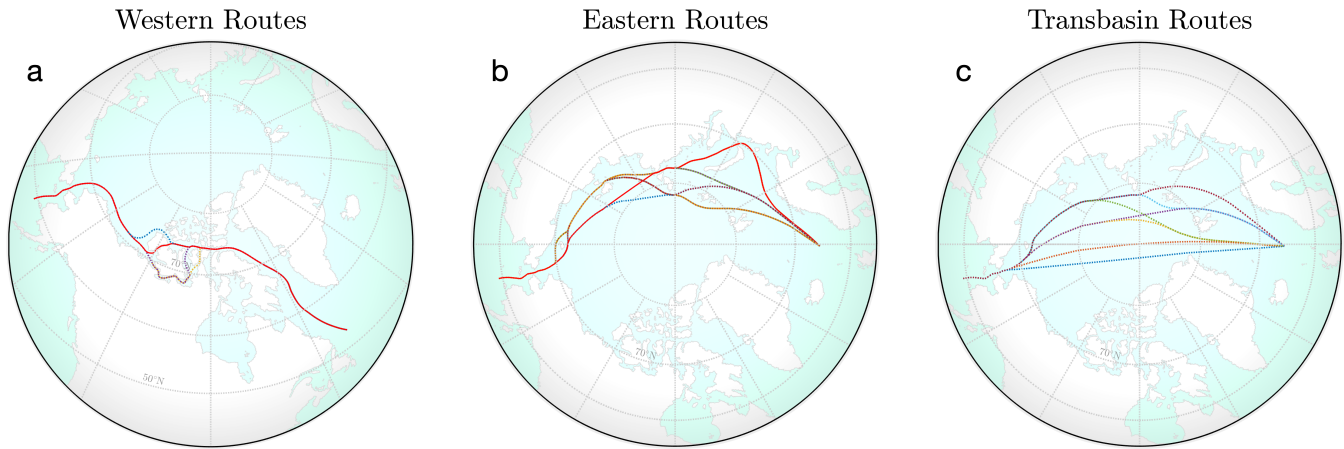


Figure 1: Twenty permutations of possible 21st century Arctic ship routes between the Pacific and Atlantic Oceans, classified into (a) western and (b) eastern coastal paths, and (c) trans-basin routes. The solid red variant of the Northwest Passage in (a), which is nominally 3921 nautical miles in length, and the red Northern Sea Route variant in (b), 4262 nautical miles long, are respectively expected to be among the most used in western and eastern hemispheres, respectively, by year 2030. The most direct (blue dashed) great circle polar route in (c) measures 3298 nautical miles between the same Arctic entry points as the red Northern Sea Route in (b).

The Arctic is transitioning to a seasonally ice-covered ocean akin to most of the Southern Ocean in the 20th century. This means that the Arctic Ocean will be covered in sea ice during winter for the foreseeable future, but with increasingly-reduced extent, thickness and increasingly-long ice-free summers after that threshold is met by 2050 (*Notz and Community, 2020*). Best estimates for the transition to ice-free September are provided in a separate answer above. Owing to the continued seasonality of sea ice, navigability needs to be framed in terms of length of the ice-free season, rather than year-round operation. Icebreakers will find it increasingly easy to navigate throughout the year in polar oceans. Vessels with IMO Polar Class 7 (PC7, also equivalent to Finnish-Swedish Class IA) are designated for operations in thin first-year ice with possible old ice inclusions. For this type of ships, no single trans-Arctic ship route will be navigable year-round in the first half of the 21st century, including in the fossil-fueled future (SSP5) scenario of CMIP6 projections (*Wei et al., 2020*). However, seasonal trans-Arctic navigability will increase this century, and for some polar classes discussed later, including Russian ARC 7 LNG tankers (PC3), uninhibited passage will be likely for at least six months of the year from the current day.

Ship routes through the Arctic can be classified into coastal and trans-basin paths, as illustrated in Figure 1. The solid red Northwest Passage variant through Prince of Wales Strait (Figure 1a) is the northernmost variant likely to become reliable in the coming decades, open for roughly 100 days a year (*he Liu et al., 2017*); other variants further south will increase in navigability beyond this benchmark based on CMIP6 data (*Wei et al., 2020*). Of all, the solid red Northern Sea Route (Figure 1b) is expected to continue to be the most viable trans-Arctic path for the longest period of time each year. This route avoids much of the variability in thick (>2 m) seasonal landfast sea ice off the Siberian coast that ships visiting Siberian ports such as Pevek may encounter, and which few Earth system models are able to simulate at the present time. Therefore, predictions about the year-round navigability of the Northern Sea Route that hugs the Siberian coast for anything other than icebreakers based on CMIP models must be treated as preliminary based purely on ice conditions. However, due to the extremely shallow water between 10 and 13 m deep in some straits along the amber dashed route in Figure 1b, this path is unlikely to be preferred by large ships, such as ARC 7 LNG tankers, regardless of ice conditions. The most direct transarctic shipping route to and from

Europe (Figure 1c) may not be seasonally ice free until after 2040 even in a fossil-fueled future (*Wei et al.*, 2020), but it offers a travel distance reduction to Europe of approximately 1100 nautical miles compared to the amber-colored Prolix Longa variant of the Northern Sea Route described above (Figure 1b).

3.2 Changes in Arctic sea ice along the Northern Sea Route

This Section includes answers to questions that focus more specifically on changes in Arctic sea ice and shipping access along the Northern Sea Route (NSR) in response to a changing climate. The answers to these questions are based on the multi-model ensemble analysis described in detail in Section 4 of this report. We focus on Polar Class 3 (PC3) vessels, which are heavily ice strengthened, but do not rise to the level of nearly-uninhibited navigability enjoyed by Russian nuclear-powered icebreakers (PC1). ARC 7 LNG tankers, including those in Sovcomflot's fleet, are classified as PC3 vessels. Some analysis is also performed for conventional or non-ice-strengthened vessels, as per IMO denomination. These ships present the highest risk in the IMO tables of Risk Index Values for operations in sea ice¹.

1) How many days of the year will the NSR be navigable, per vessel type in the future?

An estimate on the number of days per year that the NSR will be navigable in the future is beyond the scope of the current analysis except at the granularity of monthly windows. This is because our analysis is based on a multi-model ensemble which, when averaged across all models (with caveats provided below in Section 4.1) and over sufficient time, has significant statistical confidence achieved by reducing the impact of model outliers and decadal climate variability; while confidence in any one given model for any given period of time is low, confidence in the decadal ensemble mean is high. In addition, only a subset of the full model ensemble provides daily data, which is required for an analysis on the number of days of navigability. That criterion alone, which is insufficient for retaining or removing models from the ensemble, would both bias the results and lower our confidence in them. An assessment at the granularity of days per year would be better investigated via the detailed analysis of a single model ensemble in which we hold a high degree of confidence.

2) In what months (or seasons) will the NSR be navigable? When will the NSR begin to be navigable in March and April, the months Russia so far has not been able to navigate? When will Russia be able to increase its transit via the NSR during months it currently only has limited capability (May, June, December, January, and February)?

The Risk Index Outcome (RIO) plots and discussion in Section 4.6 can be used to address this question. For example, using Figures 12 and 15 below, one can ascertain that along route 6 (see Figure 2 for routes), an ARC 7 LNG tanker will be at low risk ($\text{RIO} > 0$) in December through April during the current decade (again, a granularity beyond decadal-scale means is not warranted in the current study). May will continue to entail some risk ($\text{RIO} \approx 0$) along relatively short segments of these routes (10's to 100's of nautical miles) through the end of the next decade (2030-2039). The Spring peak in risk is due to the fact that the thickness of snow-on-sea ice, and thus the albedo feedback, peaks in May. Come June, snow rapidly melts away, and thereafter the underlying sea ice becomes thinner and less concentrated. The decrease in concentration greatly reduces risk. Additional figures analogous to Figures 12 and 15 provided in the appendix can be used for similar assessments along route 20, which avoids Sannikov Strait.

¹See IMO Circular [MSC.1/Circular.1519](#)

3) What types of ships will be required? For example, when will the NSR be navigable by ARC 7 ice class vessels? When will it be navigable by conventional tankers? When will it be navigable with and without icebreaker escorts?

According to the ensemble-mean RIO values calculated here, most of the NSR will be navigable by ARC 7 vessels for the majority of the year within this decade (2020-2029; Figure 12). Polar Class 3 (PC3) ice-hardened vessels (like ARC 7 LNG tankers) can operate safely, albeit at reduced speeds, in conditions where $-10 < \text{RIO} < 0$ (e.g., as per the 50th percentile of the ensemble distribution for May of 2020-2029, shown in Figure 13). For conventional tankers (non-ice-strengthened vessels as defined above), the story is much different. With no icebreaker escorts, conventional tankers will continue to encounter dangerous or impassable conditions (they should not operate where $\text{RIO} < 0$) along many sections of most routes through the end of this decade for many months of the year. In 2020-2039, conventional tankers will be able to operate safely along route 6 from August through October (see Figure 16). By 2040-2049 this increases to August through November and, by 2050-2059, from July through November (assuming a route avoiding Sannikov Strait; Figure 17). We note that an accurate assessment of the risk reduction for conventional tankers afforded by icebreaker support is beyond the scope of this report due to variables unaccounted for in our analysis. For example, this assessment would require knowledge of the ice types and concentrations between escorted and escorting ships, as well as their operating drafts and beams. A key navigational hazard for large ships such as ARC 7 LNG carriers is their draft, which may only marginally exceed the minimum depth of Sannikov Strait, making that route either innavigable or risky, regardless of ice conditions.

4) How if at all will navigability and the ships required vary across different sections of the NSR?

To answer this question, we divide the NSR between four key passages that register the greatest localized navigational hazards. Passing from the Atlantic to the Pacific side of the Arctic, these are: 1) Kara Strait joining the Barents and Kara Seas; 2) Vilkitsky Strait joining the Kara and Laptev Seas; 3) Dmitry Laptev and Sannikov Straits between the Laptev and East Siberian Seas; 4) Passage around Wrangel Island, either to the North or through Long Strait to the South (see Figure 2). In each case, the straits provide constrictions not just for the passage of ships but also a confluence for ice that can thicken through ridging and grounding, with an associated increase in ice concentration. Due to ice grounding, conditions are affected by landfast ice, typically at less than 20 m depths, although the physics of landfast ice is seldom represented in Earth system models. The minimum depth in Dmitry Laptev Strait and its approaches ranges between 10 and 15 m, whereas the minimum depth in Sannikov Strait is around 13 m (*Pastusiak*, 2016), slightly exceeding the ARC 7 loaded draught of around 11.5 m, and for that reason our route calculations use the latter. These straits – Kara, Vilkitsky, Sannikov, and Long – are marked in Figure 2, and we now discuss the most risky elements of the NSR with reference to Figures 12, 13, and 15, and demonstrate that for ARC 7 LNG tankers traveling between Sabetta and Asia, it is desirable to completely avoid Dmitry Laptev and Sannikov Straits on routes 5 and 6, and instead follow route 20 now and into the future (Figure 2c).

Sannikov Strait typically registers as having the lowest RIO of all portions of the NSR (routes 5 and 6), and is most extreme in May for ARC 7 (PC3) vessels ($\text{RIO} \approx 0$). Similar risk is associated with passage to the west of Wrangel Island in the East Siberian Sea at that time of year. Lesser local dips in RIO occur through Vilkitsky Strait and the Kara Gate. The increased risk in the East Siberian Sea and through Sannikov Strait is largely associated with shoaling bathymetry, which are reflected in a very cool water column and associated thick sea ice in the model physics represented in the ensemble. Most models in the ensemble have no explicit landfast ice representation, which means the models' sea ice physics do not allow for the grounding of ice keels in shallow water. However, horizontal ice mechanics in the models do accommodate restrictions in navigability associated with ice confluence in narrow straits. Landfast ice physics would likely

increase the risk associated with straits above the existing predictions. We also note that tidal amplitudes in this region are among the highest in the Arctic basin, but we do not take these into account with regard to grounding risk, which RIO does not accommodate. See Section 4.7 for a longer discussion of omissions in our estimate of risk. Taking route 20 avoids many of the risks associated with the East Siberian Sea and its approaches, and from the perspective of the NSR is only undesirable when wishing to steer close to Siberian ports for point-to-point Arctic shipping or for proximity to maritime support. We note that recent monitoring of shipping activity along the NSR from the Sabetta port confirm avoidance of the Sannikov Strait².

Different sections of the NSR will experience different levels of risk at different times of year and depending on the vessel ice class. For example, in Figure 12, which shows the RIO for an ARC 7 (PC3) vessel along all routes in February and May (with the latter currently being the month with the highest risk for operations of any vessel type during the four decades analyzed), there is no risk along any route in February even during the current decade. For May, there is no risk for an ARC 7 vessel along some routes (e.g., 17 and 18) but some risk along parts of some routes (e.g., coastal routes 5 and 6). Because an ARC 7 can still operate for $-10 < \text{RIO} < 0$ (although at a reduced speed), routes 5, 6 will be navigable in May during the current decade, based on this analysis. Navigability along route 20 during the months March, April, and May of this decade will typically pose less risk compared to navigability along route 6 (compare top panels of Figures 23 through 26). These conclusions are very different for non-ice-strengthened vessels, such as conventional tankers, which would find the majority of routes impassable even in June and July of this decade (see Figure 16 and 17 for RIO values along route 6 and 20, respectively). Figure 15 shows how operation risk for an ARC 7 varies along route 6 as a function of month and for different decades (additional figures in the appendix show results and model spread for all months, both along route 6 and 20). While the question as asked is quite broad, the specifics as a function of route, time of year, decade and vessel ice class, with the extremes bounded by ARC 7 and conventional tanker, can be answered based on the more complete set of RIO plots provided in the appendix.

5) How many days will it take to navigate the entire NSR by vessel type and time of year? How many days will it take for the portions of the NSR to the east and to the west of the Yamal LNG plant, at Sabetta on the Yamal Peninsula?

The answer to the first question will vary significantly depending on route, vessel type, time of year, and decade, but can be calculated using the plots provided in the main body of the report, in the appendix, and available information about vessel performance in various conditions. Here, we provide a worked example to the second question, noting that the results will be approximate as a result of the limitations discussed in Section 4.7 below. We assume an ARC 7 vessel traveling from the Yamal Peninsular region along route 6 in May of the current decade (2020-2029). The distance from the Yamal LNG plant to the Bearing Strait is approximately 2430 NM (starting from the small black circle between the Yamal Peninsular and Severny Island in the left-hand plot of Figure 6 and counting 250 NM increments to the Bearing Strait). From Figure 12, we see that route 6 is largely unimpeded ($\text{RIO} > 0$) but for two sections of approximately 110 and 215 NM in length (325 NM total) with an RIO of around 0. For the 2105 NM of the route with $\text{RIO} > 0$, an ARC 7 can travel at open water cruising speeds³ of 19.5 knots and for the 325 NM of the route with $\text{RIO} \approx 0$ we assume reduced speeds of 5 knots (as per IMO recommendation under “elevated risk operations”). Under these conditions, the minimum total travel time would be approximately $2105 \text{ NM} / 19.5 \text{ knots} + 325 \text{ NM} / 5 \text{ knots} = 173 \text{ hours} = \mathbf{7.2 \text{ days}}$ ⁴. Under the same assumptions but in June (or alternatively, even in

²See the “MAPS” section of the [Northern Sea Route Information Office](#).

³See [Yamal LNG Plant website](#), under LNG Shipping.

⁴Factoring in an estimate for the uncertainty based on the ensemble distribution of the RIO (Figure 13), there’s a 50% chance of encountering sections of $270 + 380 = 650 \text{ NM}$ in length for which the $\text{RIO} \leq 0$, which would increase the travel time

May by 2040-2049) with an $RIO > 0$ for the entire route, the minimum travel time would be approximately
 $2105 \text{ NM} / 19.5 \text{ knots} = 125 \text{ hrs} = \mathbf{5.2 \text{ days}}$.

to $1780 \text{ NM} / 19.5 \text{ knots} + 650 \text{ NM} / 5 \text{ knots} = 221 \text{ hours} = \mathbf{9.2 \text{ days}}$.

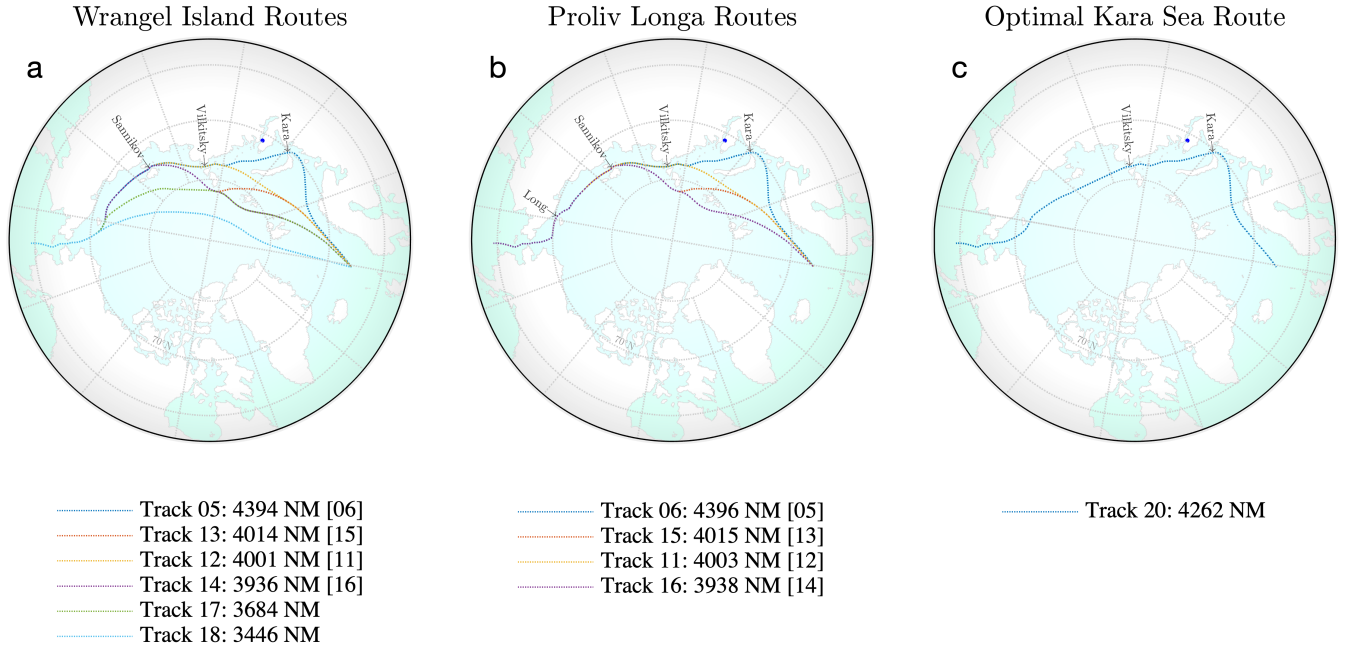


Figure 2: East Arctic shipping routes along which navigability is assessed within a subset of CMIP6 models in this report. Routes are categorized into those that pass to the north of Wrangel Island (a) and those that navigate through Proliv Longa between Siberia and Wrangel Island (b), and the optimal Kara Sea route (c), which follows an orthodrome between Vilkitsky Strait and Wrangel Island. Complementary routes split only by the path variant around Wrangel Island are signified with square brackets in the legend. The Trans-Arctic distance of each path is indicated in nautical miles (NM). The point marker on the Yamal Peninsular marks the Sabetta liquid natural gas shipping facility on the ‘Ob estuary. Important straits for navigation along the NSR are marked with the following distance from the start of route 6 on the Pacific side: Kara Strait or Gates (Karskiye Vorota; 3011 NM), Vilkitsky Strait (Proliv Vil’kitskogo; 2165 NM), Sannikov Strait (Proliv Sannikova; 1602 NM) and Long Strait (Proliv Longa; 873 NM).

4 Ensemble Analysis of Future Sea Ice Conditions Along the Northern Sea Route

In the remainder of this report, we focus on the analysis of sea ice conditions and future navigability along routes in the East Arctic shown in Figure 2, including the Northern Sea Route (NSR; routes 5 and 6) based on a multi-model, ensemble analysis of CMIP6 model outputs. We first discuss the selection of CMIP6 models used in the analysis (Section 4.1), followed by the data acquisition and reduction methods (Section 4.2). Next, we discuss the overall large-scale changes in Arctic ice cover projected by the models (Section 4.3) and the importance of accounting for a model’s native grid in our analysis (Section 4.4). We then focus on analyzing changes in sea ice concentration and thickness along the ship routes illustrated in Figure 2 (Section 4.5) and discuss and present the primary result of our report, the monthly along-route navigability according to the Risk Index Outcome (RIO) over the next four decades (Section 4.6). We finish with a discussion of the limitations of our analysis and this report (Section 4.7).

4.1 Initial Selection of CMIP6 Models

The present analysis is based on data obtained from Earth-system models submitted to CMIP6⁵. Following the study carried out by *Docquier and Koenigk* (2021), 33 models were selected from the larger CMIP6 database. This selection includes models with relevant Arctic oceanographic properties, able to reproduce historical observations (1979–2014 or 2000–2014) of sea ice area, volume and ocean heat transport (but not every model reproduces all observational metrics). The initial focus was on the high-emission scenario

⁵The **Coupled Model Intercomparison Project, sixth phase**, of the World Climate Research Programme (WCRP).

of greenhouse gases SSP⁶5-8.5, which refers to an atmospheric radiative forcing of 8.5 W/m² by the end of this century, resulting from largely unmitigated anthropogenic emissions. The associated global-mean warming for this emission scenario is $\approx 4^\circ\text{C}$ for 2081–2100 relative to the period 1995–2014. It was selected for initial analysis here because it represents the most extreme warming scenario and thus an upper-bound estimate on future reductions in Arctic sea ice concentration and thickness (although, as mentioned above, the overall sensitivity of Arctic sea ice in CMIP6 models to the particular choice of emissions scenario is relatively low).

The multi-model mean of the 33 models predicts that Arctic sea ice area and volume will reduce, respectively, by 45% and 78% in March by the end of the century, compared to the period 2015–2019. In September, the multi-model means of Arctic sea ice area and volume predict reduction factors of 90% and 98%, respectively (when comparing the same time periods). Although affected by a large uncertainty, the multi-model mean also suggests that the Arctic Ocean will become ice-free (here defined as having a sea ice area of less than 10^6 km^2) by September of 2061. Many models, however, predict an almost complete loss of sea ice by the year 2050 in September

The complete list of the initial 33 models used in this analysis is presented in Table 1. Further details on the Table entries are provided in Section 4.2.

Table 1: Complete list of models, number of ensemble members (Runs), grid type (native or re-gridded), and data frequency (Daily, Monthly) for the list of variables (1-8) given in Section 4.2.

Model	Runs	Grid	1	2	3	4	5	6	7	8
ACCESS-CM2	3	n	D	D	D	D		M		
	3	n			M	M	M			
ACCESS-ESM1-5	10	n	M	M	M	M	M			
AWI-CM-1-1-MR	1	n	D	D	D	D				
	1	n					M			
BCC-CSM2-MR	1	n	D	D	D	D				
	1	n					M		M	
CAMS-CSM1-0	2	n	M		M	M	M			
CanESM5	23	n	D							
	25	n		M						
	23	n			D	D				
CanESM5-CanOE	3	n	M		M	M				
CESM2	3	n	D	D	D	D				
	3	n					M	M	M	M
CESM2-WACCM	5	n	D	D	D	D				
	5	n					M	M		
	4	n							M	M
CNRM-CM6-1	1	n	D	D	D	D				
	6	n	M	M	M	M	M			
	1	n						M		
CNRM-CM6-1-HR	1	n	D							
	1	n		M	M	M	M	M		
EC-Earth3	8	n	D							
	20	n	M							
	8	n		M	M	M				
	12	n					M			
	5	n						M		
EC-Earth3-Veg	6	n	D							

Continued on next page

⁶Shared Socioeconomic Pathway

Table 1 – continued from previous page

Model	Runs	Grid	1	2	3	4	5	6	7	8
	6	n	M	M	M	M				
	5	n						M		
FGOALS-f3-L	1	n	M		M	M	M	M		
FGOALS-g3	4	n	M		M	M				
FIO-ESM-2-0	3	n	M		M	M	M	M		
GFDL-CM4	1	n	D	D						
	1	n	M	M	M	M	M			
GFDL-ESM4	1	n	M	M	M	M	M			
HadGEM3-GC31-LL	4	n	M	M	M	M	M	M		
HadGEM3-GC31-MM	4	n	M	M	M	M	M	M		
INM-CM4-8	1	r	M							
INM-CM5-0	1	r	M							
IPSL-CM6A-LR	6	n	D	D	D	D				
	6	n					M	M	M	M
KIOST-ESM	1	r	D	D	D	D				
MIROC6	3	n	D	D	D	D				
	1	n					M			
MIROC-ES2L	1	n	D	D	D	D				
	10	n	M	M	M	M				
MPI-ESM1-2-HR	2	n	D	D	D	D				
	2	n					M			
MPI-ESM1-2-LR	10	n	D	D	D	D				
	10	n					M			
MRI-ESM2-0	2	n	D	D	D	D				
	2	n					M		M	M
NESM3	2	n	D	D	D	D				
	2	n							M	M
NorESM2-LM	1	n	D	D	D	D				
	1	n					M	M	M	M
NorESM2-MM	1	n	D	D	D	D				
	1	n					M	M	M	M
UKESM1-0-LL	5	n	M	M	M	M	M	M	M	M

4.2 Data Acquisition and Reduction

The initial intent of the analysis required the acquisition of a number of sea ice variables from the CMIP6 database for all models reported in Table 1. Specifically,

1. the sea ice concentration (**siconc**), i.e., the fraction of a grid cell (of the sea ice model component) covered by ice;
2. the sea ice thickness (**sithick**), i.e., the average thickness of ice in the fraction of a grid cell covered by ice;
3. the sea ice velocity component in the “ x ” direction (**siu**);
4. the sea ice velocity component in the “ y ” direction (**siv**);
5. the sea ice volume per grid-cell area (**sivol**), i.e., the average thickness of ice when distributed over the entire area of a grid cell;

6. the age of sea ice since its formation in open water (**siage**);
7. the fraction of a grid cell covered by each ice-thickness category (**siitdconc**);
8. the sea ice thickness (equivalent to **sithick**) in each ice-thickness category (**siitdthick**).

The variable **sithick** is also referred to as “actual” or “floe” thickness of sea ice and represents the average thickness over the ice-covered portion of a grid cell.

In the discussion below, the variable **sivol** is referred to as “mean ice thickness” over the whole grid cell (including open water) and provides a bulk measure of the ice content of a grid cell. The pair of variables (**siu,siv**) represent the vector velocity of sea ice in a grid cell (“x” and “y” above refer to perpendicular directions on the sea ice grid).

Within the Polar Operational Limit Assessment Risk Indexing System⁷ (POLARIS), the variable **siconc** represents a primary quantity in the determination of the Risk Index Outcome (RIO), which is a linear combination of the concentrations of each ice type and the corresponding Risk Index Value (RIV) associated with each ice type. The RIV depends on the (floe) thickness of the ice and its age. Henceforth, we assume that assessment of the RIO for a particular model necessitates outputs for at least sea ice concentration (**siconc**) and sea ice thickness (**sithick**).

CMIP6 prioritized model output variables to be provided by participating groups. As a result, not all variables listed above are available for every model. Data for variables from the ocean and sea ice realms typically have monthly frequency. Daily output is also available, but only for a smaller subset of models. During the data acquisition process, priority was given to daily data. In a few circumstances both daily and monthly data were acquired.

A number of models in the database are available as an ensemble of simulations (i.e., the same simulation is repeated by applying some perturbation to the initial conditions). An ensemble allows for an estimate of the internal variability of the model. While the number of ensemble members is typically small (only 10 out of 33 models provide 5 or more ensemble members), and therefore internal variability cannot be assessed on statistical grounds, single-member simulations do not allow for any assessment (of any type) of the model internal variability. In some cases, not all variables were provided for all ensemble members, or not all variables were submitted with the same frequency. To avoid the arbitrary choice of selecting a single member of an ensemble, available variables from multi-member models were averaged.

For reasons that will be discussed below, we required that the output variables for a given model were available on the *native grid* for the ocean and sea ice model component (where they are actually computed by the model). CMIP6 allowed for model output data to be interpolated onto, and provided on, a non-native grid and for some models, outputs are not available on their native grids. Because coast lines can only be resolved at the resolution of the native model grid, ocean and sea ice covered surfaces may be “closed” in the model, and represented as part of the land component of the Earth-system model. Thus, when tracking shipping lanes along the coast or in the proximity of islands, identifying whether or not the lane crosses actual land points in the model requires access to the data on the native grid of the ocean and sea ice component. This information is inaccessible when working with data interpolated onto a secondary grid, which typically employ a uniform spacing in latitude and longitude for ease of data management. Identifying these artificial, native-grid-induced blockages along shipping route is important to our analysis because modeled sea ice variables can be strongly biased by their proximity to land.

Table 1 lists the model in the first column. The number of ensemble members is given in the second column. About one third of the models provide a single-ensemble member. The third column provides the type of grid on which the variables are provided, which is native (n) except for models INM-CM4-8, INM-CM5-0, and KIOST-ESM. Variables for these 3 models are re-gridded (r) and therefore excluded from the analysis presented in the following Sections. Variables in Table 1 are labelled 1 through 8 (corresponding to the numbering in the list above): they are marked with a “D” for daily frequency, “M” for monthly frequency,

⁷See [IMO Guidance on Methodologies for Assessing Operational Capabilities and Limitations in Ice](#), MSC.1/Circular.1519 of June 6, 2016.

and are unmarked when unavailable. A total of four models in the Table are of limited use to the analysis (and of no use for the determination of RIOs) since they do not provide any ice thickness information (i.e., none of `sithick`, `sivol`, `siitdthick` is available). Henceforth, the Risk Index Values cannot be assessed. These four models include two models that do not fulfill the grid requirement. The other two models are CanESM5-CanOE and FGOALS-g3. In total, five of models in Table 1 cannot be used for the current analysis. Note that for practical purposes variables `sithick` and `sivol` are related to `siconc` by `sivol=sithick×siconc`. Because they are listed as “non-priority” variables by CMIP6, `siage`, `siitdconc` and `siitdthick` are only available for a small number of models (15 for `siage` and 8 for the others).

For purposes of data processing and management, a pipeline for data reduction was developed with the purposes of removing both spatial and temporal information not relevant to the analysis. In particular, the time domain of the data was restricted to the period 2020–2060. The data were then further sub-set in space by extracting only the part of the ocean and sea ice grids that included latitudes $\geq 60^\circ\text{N}$. This sub-setting reduced the size of the acquired data-set by a factor of about 6.

Multi-model mean projections, based on averages performed across all available models, assume that models are all equally plausible. Clearly, when combining information from single-member and multi-member ensembles, the result may be biased toward models with many ensemble members. To remove this bias, ensemble averages of all variables were carried out for all models with a multi-member ensemble. In this way, when averaging across all models, there is only one instance per model.

4.3 Future Arctic Ice Cover

Figure 3 shows the concentration of Arctic ice in September, as predicted by three different models (as indicated) averaged over the decades: 2020–2029 (left), 2030–2039 (center), and 2050–2059 (right). Models consistently indicate a reduction of future Arctic sea ice. However, as anticipated above, the inter-model spread of ice coverage projections is substantial. Nonetheless, the uncertainty derived from multi-model ensemble statistics can be relatively well characterized given the large number of models in the initial selection presented in Section 4.1. Therefore, the uncertainty in the RIO derived from the multi-model ensemble can be characterised as well.

However, the uncertainties computed from cross-model statistics are meaningful only under the assumption that they are comparable to, or larger than, the combined uncertainty arising from the internal variability of each model. Internal variability of an Earth-system model is an intrinsic property of the model that stems from the chaotic nature of the system and finite precision arithmetic applied in numerical computations. For the cases illustrated in Figure 3, internal variability is either unknown (model CNRM-CM6-1-HR, in the middle panels, is a single-member simulation) or known only qualitatively at best (the other two models are two- and three-member simulations). As an example, Figure 4 shows the maximum (top) and minimum (bottom) sea ice concentration at each grid-cell for three different model ensembles. The figure illustrates the maximum range of variability within a single model, for three models with a similar number of ensemble members (between 4 and 6). By using a multi-model ensemble of 28 members, we can represent internal variability and model uncertainty at the same time (*Slingo and Palmer, 2011*).

4.4 Grid Blockages of Ship Routes

Eleven possible Arctic ship routes, including eastern coastal and trans-basin paths, are considered in this analysis (see Figure 1). Herein, routes are numbered according to variations of their path, as detailed in the following list.

Route 5. Northern Sea Route: Kara Strait Passage and Wrangel Island Detour;

Route 6. Northern Sea Route: Kara Strait Passage and Proliv Longa (Long Strait) Passage;

Route 11. Northern Sea Route: Kara Sea Shortcut and Proliv Longa Passage;

Route 12. Northern Sea Route: Kara Sea Shortcut and Wrangel Island Detour;

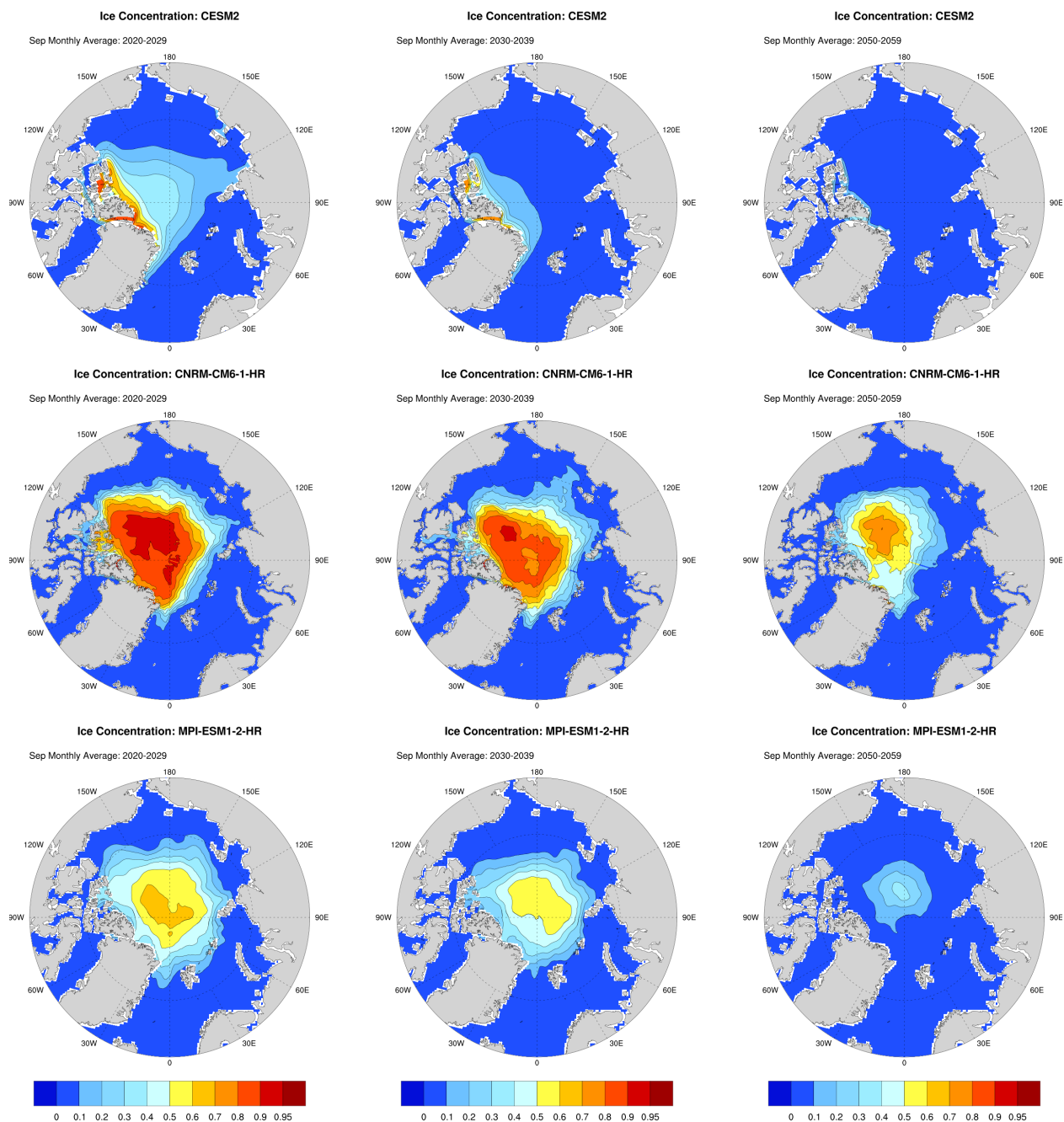


Figure 3: September average sea ice concentration for three different decades, 2020–2029 (left), 2030–2039 (center), and 2050–2059 (right), as projected by three different models (see Table 1).

Route 13. Northern Sea Route: Siberian Coastal Route with Franz Josef Land Shortcut and Wrangel Island Detour;

Route 14. Northern Sea Route: Siberian Coastal Route with Svalbard Shortcut and Wrangel Island Detour;

Route 15. Northern Sea Route: Siberian Coastal Route with Franz Josef Land Shortcut and Proliv Longa Passage;

Route 16. Northern Sea Route: Siberian Coastal Route with Svalbard Shortcut and Proliv Longa Passage;

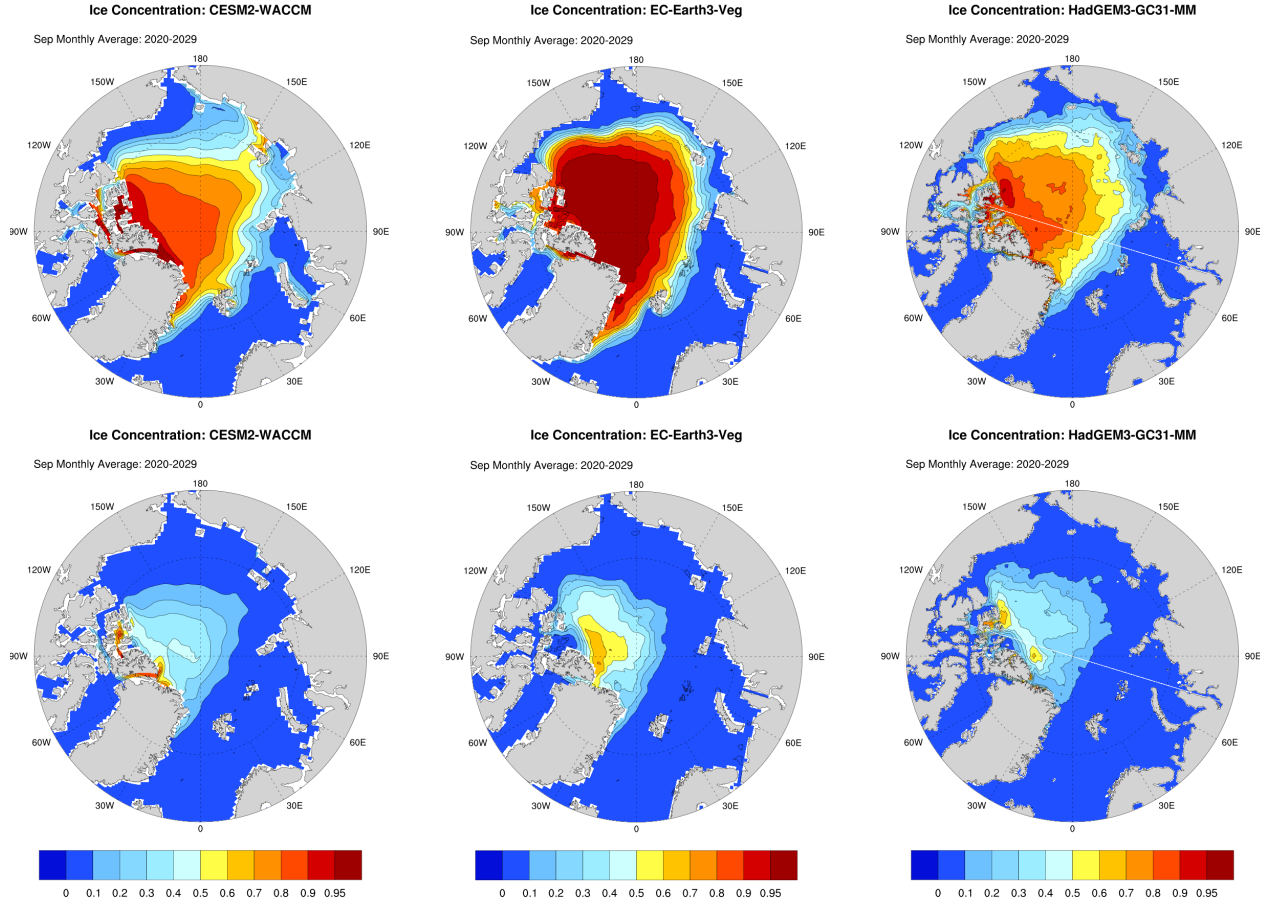


Figure 4: Internal variability of sea ice concentration in three different models (from left to right, as indicated) averaged over the month of September in the decade 2020-2029. Top panels indicate the maximum concentration in the ensemble at each grid cell. Bottom panels indicate the minimum value. The models have 5 (left), 6 (center) and 4 (right) ensemble members (see Table 1).

Route 17. Northern Sea Route: Siberian Coastal Route with Svalbard Shortcut;

Route 18. Arctic Ocean Route: Fram Strait Detour.

Route 20. Northern Sea Route: Low Risk via Kara Gate.

Of the routes listed above, route 5 and 6, which only differ around Wrangel Island, more closely represent the path of Northern Sea Route. Distances are always referenced to a common point of origin in the the Bering Sea, where all routes start. The routes have ending points (in close proximity) in the Atlantic Ocean. Because of limited grid resolution in the model ocean and sea ice components, coastal portions of the true routes are susceptible to grid-scale “blockages”, i.e., they can pass through geographical coordinates that the models associate with land rather than ocean. These route blockages are identified for all models and ship routes in order to ascertain that they do not artificially affect (in a statistical sense) ice formation and accumulation compared to those models that have open paths.

Ship routes are sampled at intervals of one nautical mile (1852 metres). For each position along a route, the closest grid cell is found (i.e., the point at which model variables are centered) and associated with that route point. If that grid cell falls outside of the ocean domain, that point on the true route is considered blocked on the models ocean and sea ice grid. In general, since grid-cell size is typically much larger than one nautical mile, several to many consecutive points along a route may be associated with the same model grid cell (and thus model variables may be identical for multiple points along a given route).

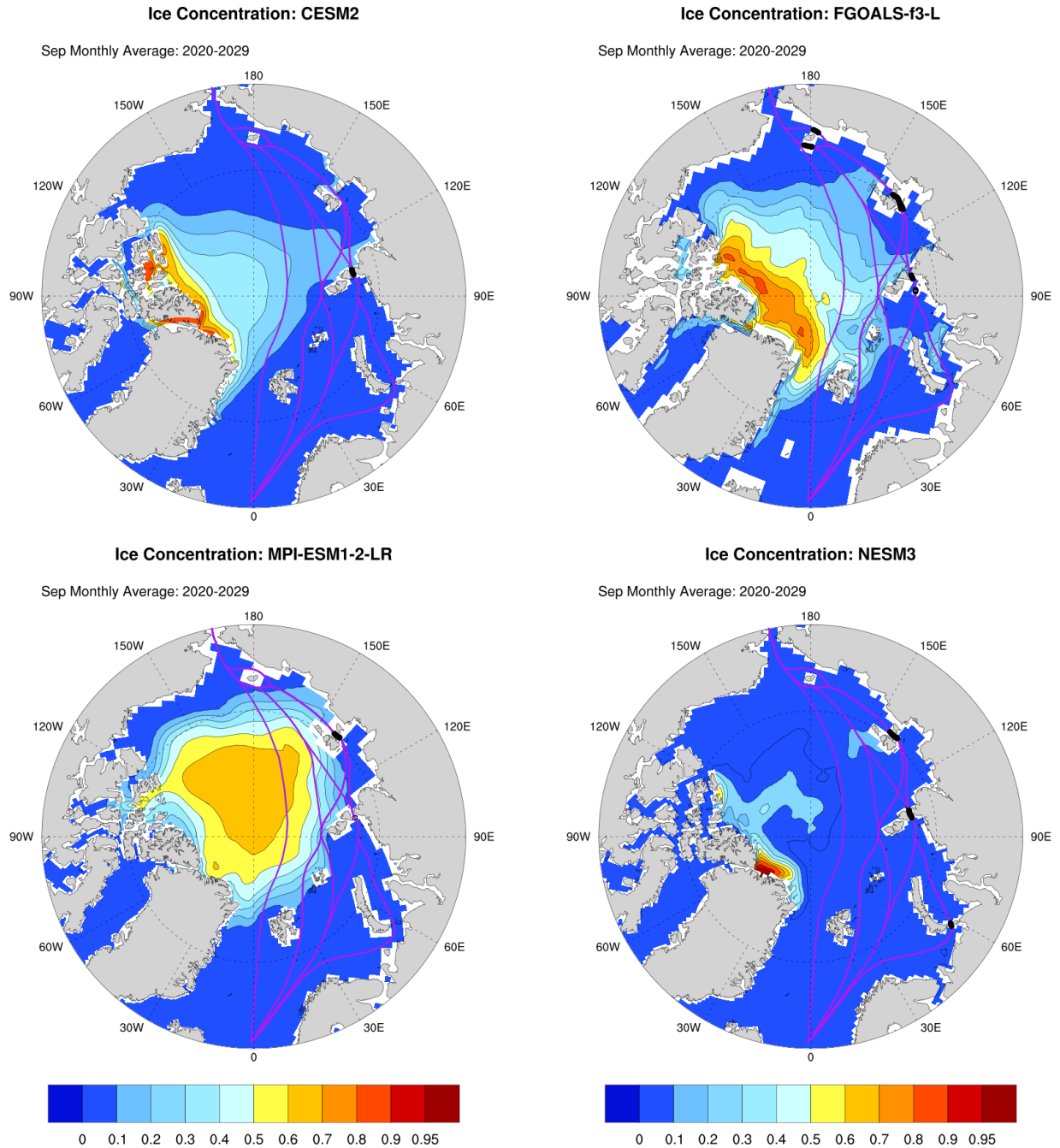


Figure 5: Examples of models in which the land mask blocks some ship routes. The color scale renders sea ice concentration (averaged for the indicated period); purple lines indicate the routes and black dots mark blockage locations.

Figure 5 illustrates all eleven ship routes (purple curves) overlain on ice concentration maps for four models whose ocean and sea ice grids lead to blockages along some routes (blockages are indicated in the figure by black dots). Grids often present blockages for routes along Kara Strait, Vilkitsky Strait, Sannikov Strait, and Long Strait (for increasing east-ward latitude). These passages are about 27 NM (50 km) wide, except for the wider 76 NM (140 km) Long Strait. Of the routes identified in the list above, route 6 crosses all four of these problematic straits. Only route 17 and route 18 avoid all of these narrow passages.

Table 2: Grid Blockages along Ship Routes

Model	Res	05	06	11	12	13	14	15	16	17	18	20
ACCESS-CM2	250											
ACCESS-ESM1-5	250											
AWI-CM-1-1-MR	25											
BCC-CSM2-MR	100	119	118	119	119	119	119	119	119			
CAMS-CSM1-0	100											
CanESM5	100											
CESM2	100	41	42	41	41							41
CESM2-WACCM	100	41	42	41	41							41
CNRM-CM6-1	100											
CNRM-CM6-1-HR	25											
EC-Earth3	100											
EC-Earth3-Veg	100											
FGOALS-f3-L	100	243	229	229	244	185	185	170	170	60		109
FIO-ESM-2-0	100	41	42	41	41							41
GFDL-CM4	25	4	5	4	4	4		4				4
GFDL-ESM4	50	41	38	30	31	20	18	21	18			21
HadGEM3-GC31-LL	100											
HadGEM3-GC31-MM	25											
IPSL-CM6A-LR	100											
MIROC6	100	45	44	37	36	36	36	36	36			8
MIROC-ES2L	100	45	44	37	36	36	36	36	36			8
MPI-ESM1-2-HR	50											
MPI-ESM1-2-LR	250	54	53	54	52	49	49	50	50			3
MRI-ESM2-0	100											
NESM3	100	159	162	135	134	73	73	73	73			89
NorESM2-LM	100											
NorESM2-MM	100											
UKESM1-0-LL	100											

Details on the blockages along the eleven ship routes are provided in Table 2. The second column lists the nominal resolution of the ocean and sea ice grid in kilometers (km) for each model. Since the majority of the models apply non-uniform or unstructured (in one case) grids, the horizontal extent of grid cells varies. Therefore, the nominal resolution is only indicative of the average grid-cell size. The Table lists, for all route identifiers, the number of points along a route that are closed to the ocean grid by land. No entry indicates a route with no artificial (grid scale) blockages. Since the ship routes have a regular sampling of one nautical mile, any non-zero entry provides the length of the route segment(s) that are blocked by land. For example, referring to Figure 5, routes closed in CESM2 account for a length of about 42 NM (77 km) (for all routes crossing the Vilkitsky Strait), comparable to its nominal grid resolution. Notice that for non-uniform and unstructured grids, even if the nominal resolution of a model is coarser than that of other models (e.g., compare ACCESS-CM2 and NESM3) some grid cells are nevertheless small enough to accurately capture a particular passages⁸.

As a reference for geographical locations and distances along routes, Figure 6 shows coastal (left) and trans-basin routes (right) with distance markers along each route. The larger circles are 500 NM (926 km) apart whereas the smaller black circles are 250 NM (463 km) from the larger ones. The routes in the left

⁸We note that, for models with a nominal resolution ≥ 50 km and all-open routes, it is likely that the ocean and sea ice grids were designed with the intent of keeping these coastal passages open. Hence, these modeling agencies may have a particular interest in Arctic climate and/or changing sea ice conditions.

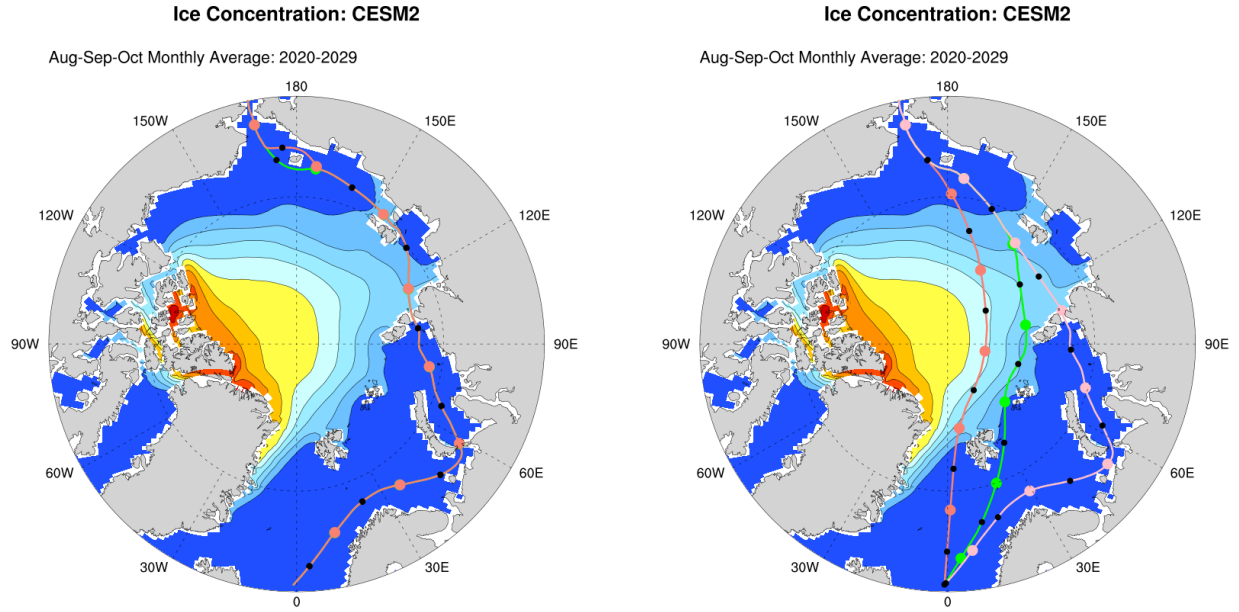


Figure 6: The coastal routes 5 (green) and 6 (orange) are shown in the left panel while route 17 (green), route 18 (orange), and route 20 (pink) are illustrated on the right. The large circles are 500 NM apart and smaller black circles are 250 NM from the larger circles. Route 6 crosses four major straits along the North Siberia coast: Long (873 NM from the Pacific side of the route), Sannikov (1602 NM), Vilkitsky (2165 NM), and Kara (3011 NM). route 20 crosses Vilkitsky and Kara straits, but the route proceeds North of Anzhu Islands, avoiding the high-risk Sannikov Strait. The color scale renders sea ice concentration, averaged over the months of August, September, and October, for the indicated years.

plot more closely follow standard NSR shipping lanes. Route 20 in the right plot deviates from route 5, between Vilkitsky Strait and Wrangel Island, by passing North of Anzhu Islands. The shipping traffic along this latter route, from Kara Sea toward East Asia, has increases significantly over the past few years.

4.5 Ice Concentration and Thickness along Ship Routes

The reduced variables were extracted at each route segment for all routes. Variables are centered at given latitude-longitude positions on a model grid, which can also be considered as the reference coordinates of the grid cells. The value of a variable at a route point is that of the grid cell whose reference position is the closest to the route point. Although the ocean and sea ice grids differ across models, this procedure allows quantities from all models to be located at the same locations on a given route segment and, therefore, to easily perform a cross-model statistical analysis.

Of the ship routes considered here, route 6 in the list above is the only one that crosses all four main straits along the North-Siberia coast, where grid blockages tend to occur. The sea ice concentration along this route is plotted in the top panels of Figure 7 as an average from the entire set of models in Table 2 (28 models). Note that route 5 overlaps route 6 for most of its course, except for passing north of Wrangel Island. In the Figure, the blue lines represent the mean values (of the model sample) at each route point and the shaded regions represent the range of uncertainty as quantified by the standard error of the mean (i.e., the standard deviation of the sample divided by the square root of the sample size) at each route point⁹. The data are for the month of September and are averaged over the decades 2020-2029 (left) and 2050-2059 (right). As mentioned above, distances along the route are measured from the Bering Sea. The bottom panels show the floe ice thickness along the route for the same periods. As reported in Table 1, this thickness is not directly available for all models. Therefore, within a model, the bottom panels use either

⁹In statistics, the standard error of the mean provides a measure of how much a sample mean deviates from the actual mean of a population (of which the sample is a representation). The standard deviation of the sample provides a measure of the dispersion of values within the population.

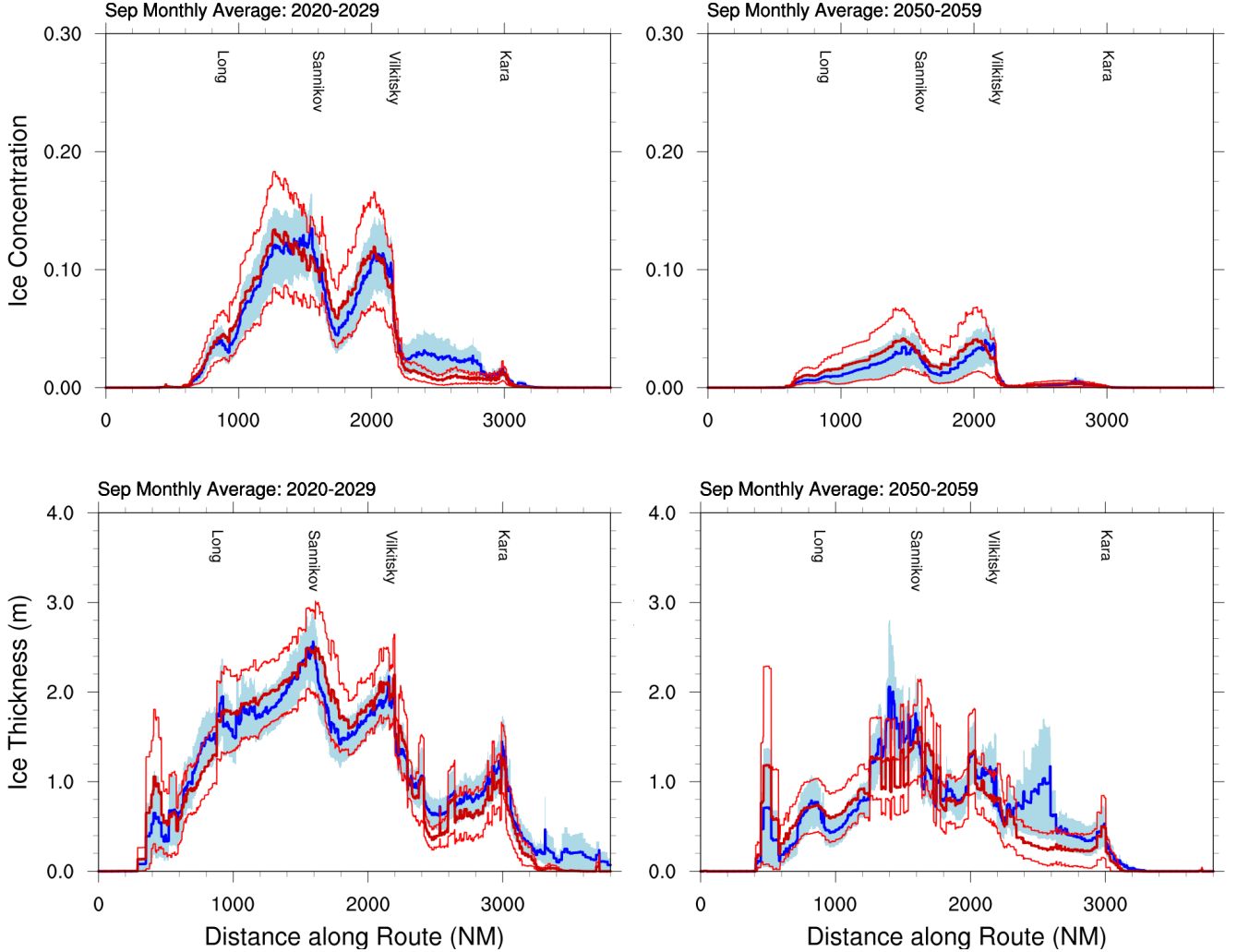


Figure 7: Sea ice concentration (top) and floe thickness (bottom) along route 6, resulting from the average including all models in Table 2 (blue curves). Distances are measured from the Pacific side of the route, which crosses all major straits, as marked by labels. The shaded regions represent the uncertainty as quantified by the standard error of the mean. The red curves indicate the same quantities, but averaged over the sub-set of models that excludes those in which the route is blocked by land cells. Left and right panels refer to mean values in September for two different decades, as indicated.

`sithick` (when provided) or `sivol/siconc` (calculated, when `sithick` is not provided).

In models with land cells along the routes, information is missing at some route points. Blue lines and shaded regions automatically exclude those route points for models with blockages. In the bottom-left panel of Figure 7, the relative maxima in ice thickness occur in the proximity of straits: Bering Strait (at ≈ 430 NM or ≈ 800 km from the beginning of the route), Long Strait (at ≈ 870 NM or ≈ 1600 km), Sannikov Strait (at ≈ 1600 NM or ≈ 3000 km), Vilkitsky Strait (at ≈ 2160 NM or ≈ 4000 km), and Kara Sea/Strait (at ≈ 3010 NM or ≈ 5600 km). Figure 7 also shows the average quantities for the sub-set of models for which no blockages exist (17 models), with the mean represented by thick red lines and the standard error represented by thin red lines.

As mentioned above, land cells along a route may affect ice formation and/or accumulation in the proximity of route blockages. The most notable differences in the top panels of Figure 7 occur in the mean values of the earlier decade, at distances between ≈ 2200 NM (or ≈ 4100 km) and ≈ 2800 NM (or ≈ 5200 km), in the

Kara Sea.

Along this route segment, the ice concentration obtained from the complete set of models is somewhat higher than that resulting from the sub-set of models with no blockages. Given the length of the route segment in which differences are observed, this suggests that the discrepancy arises from model biases rather than from the presence of grid blockages. In fact, in this particular case, most of the difference is caused by one model, BCC-CSM2-MR (present in the complete set). We also note that the differences discussed involve ice concentration values of less than $\approx 5\%$.

The differences in floe thicknesses illustrated in the bottom panels of Figure 7 are generally consistent with those in sea ice concentration. The average behavior is generally similar. In the earlier decade, some (marginal) differences do occur in the proximity of straits, e.g., between ≈ 650 NM (or ≈ 1200 km) and ≈ 870 NM (or ≈ 1600 km, in the Long Strait) and in the Kara Sea/Strait. Differences observed between ≈ 3200 NM (or ≈ 6000 km) and ≈ 3800 NM (or ≈ 7000 km) in the Barents Sea, in the left panel, and the peaks at ≈ 1400 NM (or ≈ 2600 km) and ≈ 2500 NM (or ≈ 4700 km), in the right panel, are largely produced by model BCC-CSM2-MR. It should be noted that large peaks in floe thickness corresponding with low sea ice concentrations (as also seen in Figure 7) do not significantly limit ship operations because the Risk Index Values are weighted by ice concentration in the calculation of the Risk Index Outcome, as discussed below in Section 4.6 (i.e., while thick ice may exist within a grid cell, the chances of encountering it are low).

Not surprisingly, both sea ice concentration and thickness in Figure 7 show somewhat larger mean errors for the sub-set of models that excludes those with grid blockages, a direct consequence of the smaller sample size. The trend can be opposite, but clearly not significant, in open water.

Figure 8 shows mean sea ice thickness (**sivol**) projections for three decades and six different routes (by pairs). Data are averaged for the month of September across all models in Table 2. The Figure provides quantitative information on the statistical error on sea ice volume (per unit area, i.e., the product **siconc** \times **sithick**) along the routes, as indicated by the shaded regions and the thin orange lines. While the spread of model values, that is, the standard deviation of the model sample (not shown) at any position along the routes can be substantial, the mean values are significantly better constrained.

Considering all routes, when sea ice concentration is greater than 0.15, the relative error on concentration (standard error divided by value) ranges from ≈ 0.1 to ≈ 0.5 in the first decade (and similarly for variable **sivol**). The statistical error on the mean values of the floe thickness is less than ≈ 0.3 (applying the same threshold on sea ice concentration). As expected, larger errors tend to be associated to lower values of the variables. In later decades, larger fractions of the ship routes fall beneath the 0.15 concentration. Nonetheless, relative errors remain comparable to those of the first decade.

A summary of the sea ice concentration and floe thickness along all routes is shown in Figures 9 and 10, respectively. Each value represents the mean from all the models in Table 2 (thicker lines) and from the sub-set of models in which those with grid blockages are removed (thinner lines). Data are averaged over a decade, as indicated, in the month of September. Although the floe thickness can be larger than 1 m along substantial segments of all routes $\gtrsim 1100$ NM (or $\gtrsim 2000$ km) even in the last analysed decade, sea ice concentration is $\lesssim 0.3$ already during the first decade (except for the trans-basin route 18). By 2030-2039, sea ice concentration becomes $\lesssim 0.2$ and $\lesssim 0.35$ for route 18. Consistent with the discussion above for the coastal path route 6 (see Figure 7) and as illustrated in Figure 9, the differences in estimates of sea ice concentration are only marginally different, for all routes, when including or excluding models with land cells along the routes. The same is generally also true for the floe thickness along the routes, although differences can be locally more significant along some segments of some routes. Additional information on sea ice concentrations along other routes, for various months and over the next four decades is provided in Figures 20, 21, and 22 of the appendix.

4.6 Risk Index Outcome

POLARIS, the Polar Operational Limit Assessment Risk Indexing System, was developed by the IMO to assess the type of operations and operational limitations of vessels navigating through sea ice. Within

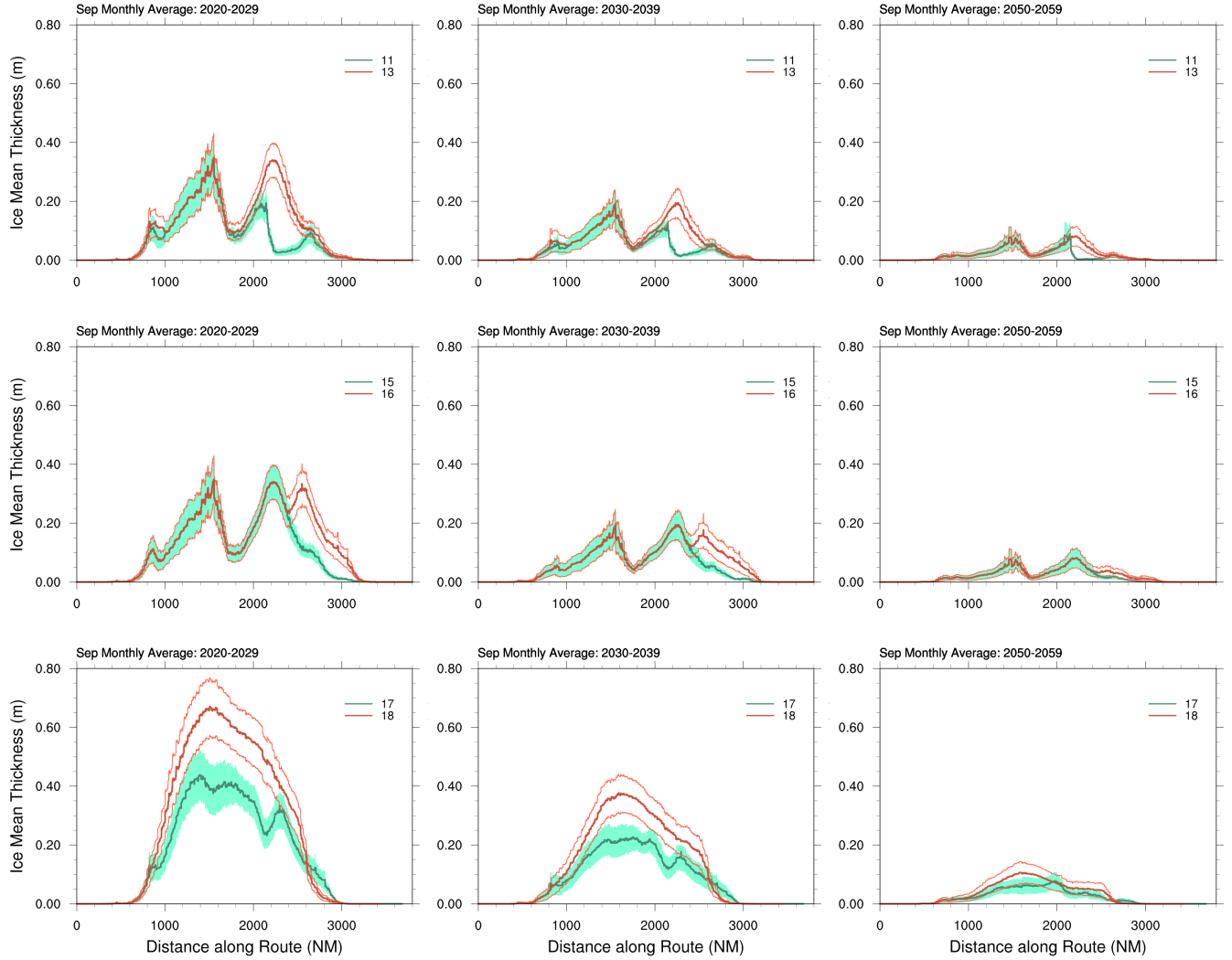


Figure 8: Sea ice mean thickness (*sivol*) in September along selected ship routes (as indicated by the identifier in the legends), from the Bering Strait to the Atlantic ocean, averaged in three different decades (left to right). The mean thickness is a measure of the ice volume in a region divided by the area of the region. The thickness is averaged using all models listed in Table 2. The shaded regions and thinner lines represent the standard error of the mean values (thicker lines).

POLARIS, the evaluation of the risks posed to a ship by various ice conditions is related to the ship's assigned ice class. POLARIS assigns a scale of Risk Index Values (RIVs) to a vessel based on its ice class and on different ice regimes. Ice classes in POLARIS include Polar Classes¹⁰ ranging from PC1 (year-round operation in all polar waters) to PC7 (summer and autumn operation in thin first-year ice with some old ice inclusions) as well as Finnish-Swedish ice classes (IA Super, IA, IB, and IC), primarily intended for merchant and cruise-ferry ships. POLARIS also defines RIVs for vessels without an assigned ice class (referred to as non-ice-strengthened ships). The ice classes ARC 9 to ARC 4, assigned by the Russian Maritime Register of Shipping, can be considered equivalent to the Polar Classes PC1 to PC7, with a one-to-one correspondence except for ARC 5, which corresponds to Polar Classes PC5-6¹¹. By convention, RIVs decrease (transitioning from positive to negative values) as risks increase within a given ice class. For example, a PC7, or IA ice class vessel (whose RIVs are very similar) navigating through first-year ice less than 1 m thick have a RIV of 0, which represents the limit for normal operations. In the remainder of this

¹⁰See IMO Circular [IMO MSC.1/Circular.1519](#) for assessing ship operational capabilities in ice.

¹¹Bureau Veritas, "Ice reinforcement selection in different world navigation areas", NI543 R01.

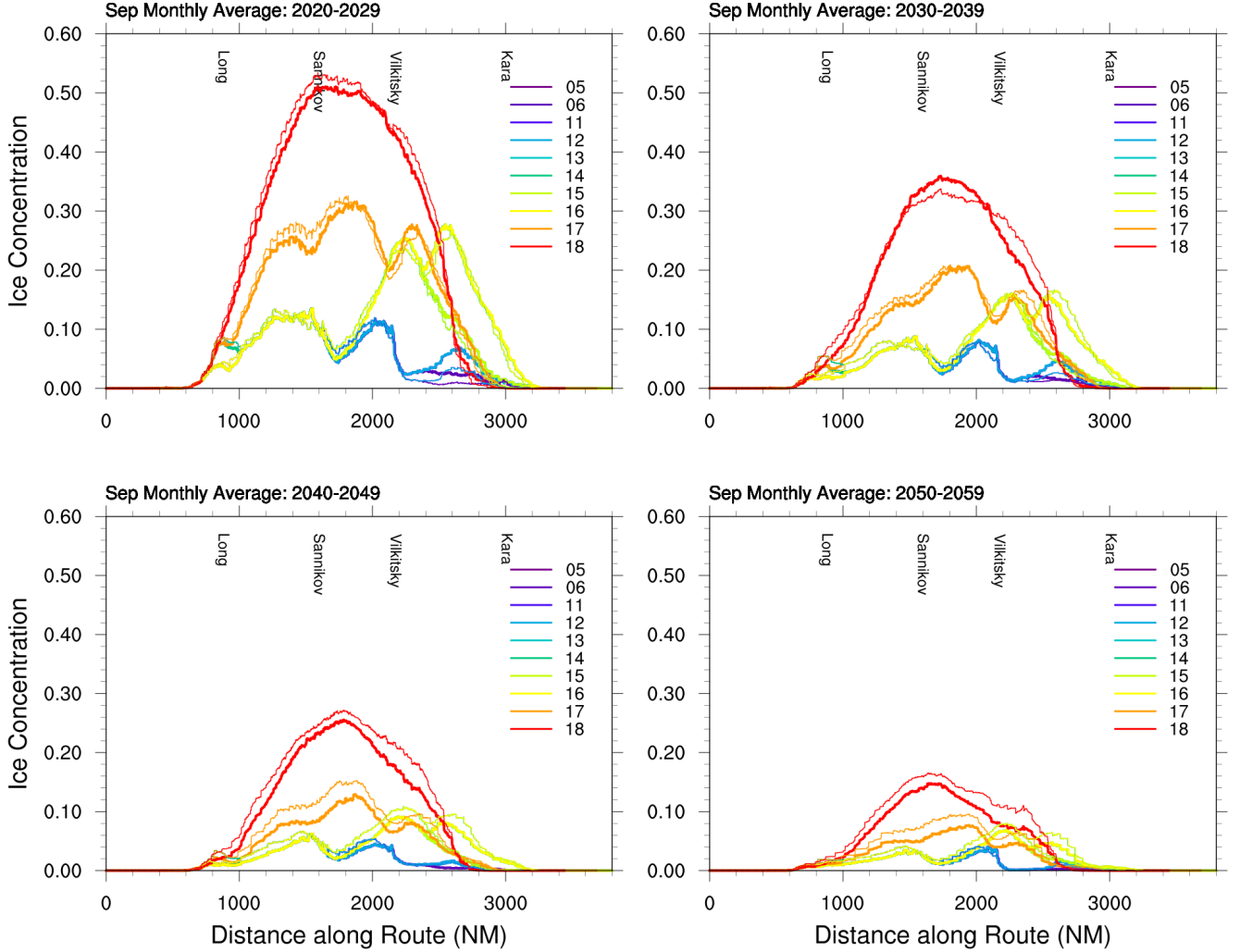


Figure 9: Sea ice concentration (`siconc`) along all ship routes (as numbered), from the Bering Strait to the Atlantic ocean. Each value represents the mean from all models in Table 2 (thicker lines) and from the sub-set in which models with grid blockages are removed (thinner lines). Data are for the month of September, averaged on a decade, as indicated. The four main straits along the Siberian coast are marked, using distances along route 6, which crosses all of them.

document, we will only analyse the operational limitations of vessels with ice class PC3, equivalent to the ARC 7 ice class, and of non-ice-strengthened ships (as defined by the IMO in terms of RIVs). To give an idea of the differences between these two types of ships for navigation in sea ice, the limit for normal operations of a PC3 vessel is reached when breaking through ≈ 2 m-thick ice whereas, for a non-ice-strengthened ship, this limit is reached in ≈ 15 cm-thick ice.

The RIV constitutes the basis for the definition of the Risk Index Outcome (RIO), which POLARIS uses to assess types and limitations of ship operations in sea ice. The determination of the RIO for navigation in an area with the presence of N different ice types, including open water, proceeds by associating a RIV to each ice type based on its thickness and age. The N RIVs are then added using the concentration of the ice types, with C (the fraction of the area they cover) as a weight, so that (by convention) $\sum_N C_n = 10$.

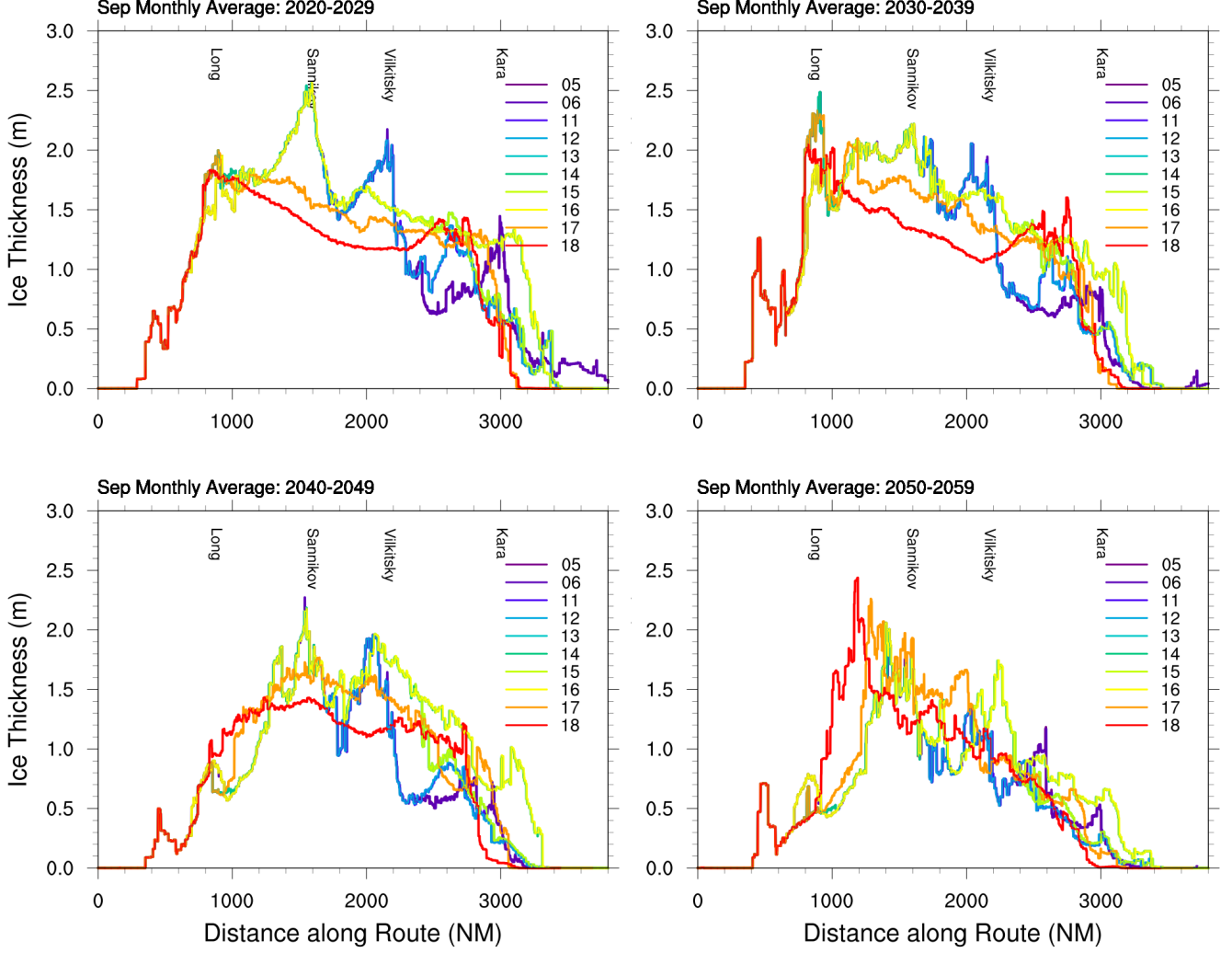


Figure 10: Same as in Figure 9, but for the actual (floe) thickness of sea ice (`sithick`) and all models in Table 2. Actual thickness and mean thickness (see Figure 8) converge to the same value as the sea ice concentration approaches to one.

The Risk Index Outcome is then

$$\text{RIO} = \sum_{n=0}^{N-1} C_n \times \text{RIV}_n. \quad (1)$$

For practical purposes, in this analysis a RIO value is evaluated at each route point using values of the ice variables associated to that point (i.e., the length across the “area” is defined by two consecutive route points). Since the variables `siconc` and `sithick` provide only one value each per grid cell (which are then associated to a route point), there are only two ice types per area (including open water). Therefore,

$$\text{RIO} = C_0 \times \text{RIV}_0 + C_1 \times \text{RIV}_1, \quad (2)$$

where RIV_0 and RIV_1 are the Risk Index Values assigned for navigation in ice-free and in ice-covered water, respectively, and the re-scaled concentrations are such that $C_0 + C_1 = 10$. For all ice classes (and non-ice-strengthened vessels), the value $\text{RIV}_0 = 3$ is assigned, such that (henceforth) the maximum RIO score is 30 (the minimum depends on the vessel’s ice class).

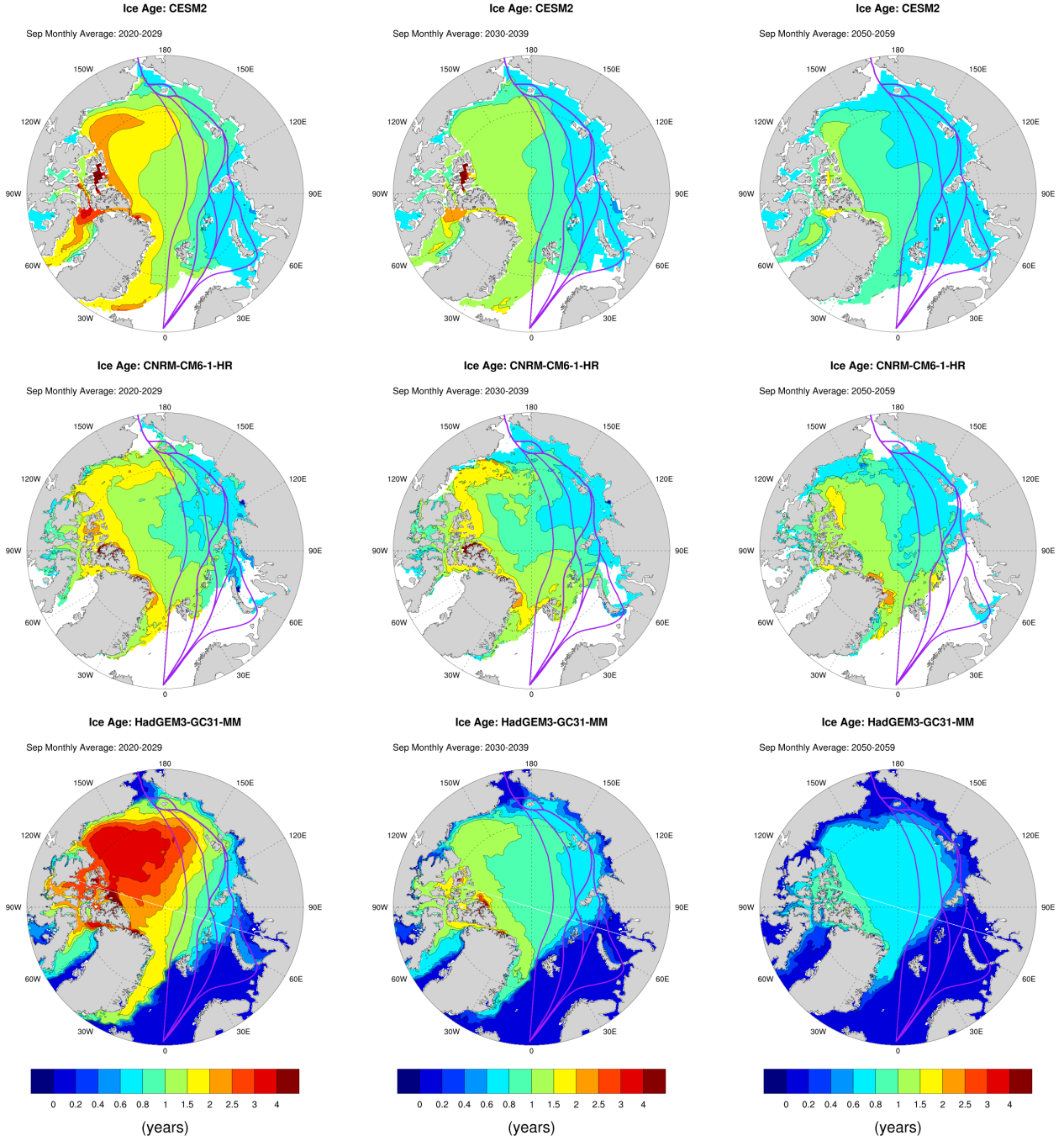


Figure 11: sea ice age in September averaged over three different decades as predicted by three different models (see Table 1). The age is counted since formation in open water.

An improvement on the procedure adopted herein to compute the RIO can be obtained by replacing the bulk variables `siconc` and `sithick` with the category variables `siitdconc` and `siitdthick`. Instead of grouping together all ice-thickness categories in a grid cell, these latter variables provide detailed information of various ice-thickness types co-existing within a grid cell and would therefore allow for the application of Equation (1) instead of the more approximate Equation (2). In practical terms, however, results from such a procedure would need to be combined with the more simple estimate, Equation (2), since only 8 models in Table 1 provide the ice-thickness category variables. Nonetheless, the two estimates together may generally improve risk assessments of navigability in Arctic ship lanes.

The risk to vessels posed by medium-to-thick ice varies significantly if the ice is older than about one year. For examples, non-Polar Class vessels have associated non-negative RIVs only in “medium” to “thin” first-year ice. About half of the models included in Table 2 provide ice age information, and some maps are presented in Figure 11. In these maps, the ship routes cross mostly first-year (or younger) ice, although some segments intercept multi-year ice during the 2020-2029 decade. The conversion from ice thickness to RIV adopted herein always assumes that ice thicker than 1.7 m is second-year (or older) ice.

The RIO score is used to determine the operational limitations of ships navigating independently (i.e., not under icebreaker escort) according to the following criteria:

- $\text{RIO} \geq 0$ defines “normal operation” for all ice classes,
- $-10 \leq \text{RIO} < 0$ defines “elevated operational risk” for PC1–PC7 ice classes.

In an “elevated operational risk” situation, vessels with an ice class PC3–PC5 are recommended to limit their speed to 5 knots (11 hours of navigation per 100 km). Ships with an ice class below PC5 are recommended to reduce their speed to 3 knots (18 hours of navigation per 100 km). For non-Polar Class vessels, a negative Risk Index Outcome identifies “operations subject to special consideration”, which ought to be avoided for route planning purposes. If the assessment of the RIO is made during transit, it is recommended to not proceed or to seek an alternate route.

Calculations of RIOs along all routes considered herein are illustrated in Figure 12, assuming a Polar Class 3 vessel (equivalent to an ice class ARC 7), for the months of February (top) and May (bottom), as averages in the decades 2020-2029 (left) and 2030-2039 (right). Shading along route 6 (which crosses all major straits) represents the standard error of the mean for the RIO assessment (providing a measure of its uncertainty). The threshold for normal operations is exceeded in the month of February, already in the first decade, along all routes. However, in the months of May (but also in April and March), the coastal routes crossing Long Strait (at ≈ 870 NM or ≈ 1600 km) and Sannikov Strait (at ≈ 1600 NM or ≈ 3000 km) have ≈ 0 or negative RIOs. Ship operations through Vilkitsky Strait (at ≈ 2160 NM or ≈ 4000 km) do not appear to pose risks (for this class of vessels) according to the models and to IMO guidance. The situation appears to improve, for navigational purposes, in the following decade. Ship routes that avoid both Sannikov and Long straits fare better in terms of RIOs.

In this analysis, the Risk Index Outcome at each route point is obtained from the mean of the distribution of model values (28 or less, depending on grid blockages, see Table 2). The dispersion of model values is estimated as “interquartile” range of the distribution, obtained from the difference between the third quartile (75th percentile) and the first quartile (25th percentile) of the probability predicted by the distribution of values. The interquartile is a measure of the statistical dispersion of the sample, accounting for the middle 50th percentile of the distribution. The interquartile range is typically considered a more robust estimate of a sample spread, compared to the standard deviation, in the presence of extreme “outliers” (although outliers were neither isolated nor defined in this analysis). Practically, this range can be interpreted as the distance between the median of the upper half of the model values and the median of the lower half of the model values at each route point. Figure 13 shows such an estimate for the RIO along route 6 (with distances measured from the Pacific side of the route), in the months of December and May, for four decades. The shading illustrated the interquartile range of the underlying distribution of values (note that the half-width of the shaded region can be larger or smaller than the standard deviation of the model values). Figure 14 is the equivalent of Figure 13, but for sub-set of models in Table 2 that excludes the ones in which the route is blocked by land cells.

Figure 15 shows RIOs estimates for the coastal route 6, for various winter and spring months, in the decades 2020-2029 through 2050-2059 (as indicated), applied to PC3 or ARC 7 vessels. The most risky months appear to be April and May, during which the RIO is close to zero, or marginally negative, along the route segments crossing Sannikov and Long straits, during the first decade. These types of ships would be subject to an “elevated operational risk” and, therefore, would need to navigate at reduced speed and/or seek an escort. The second decade poses less risks to navigability. Operations during the last two decades are essentially risk-free for PC3 (or ARC 7) vessels.

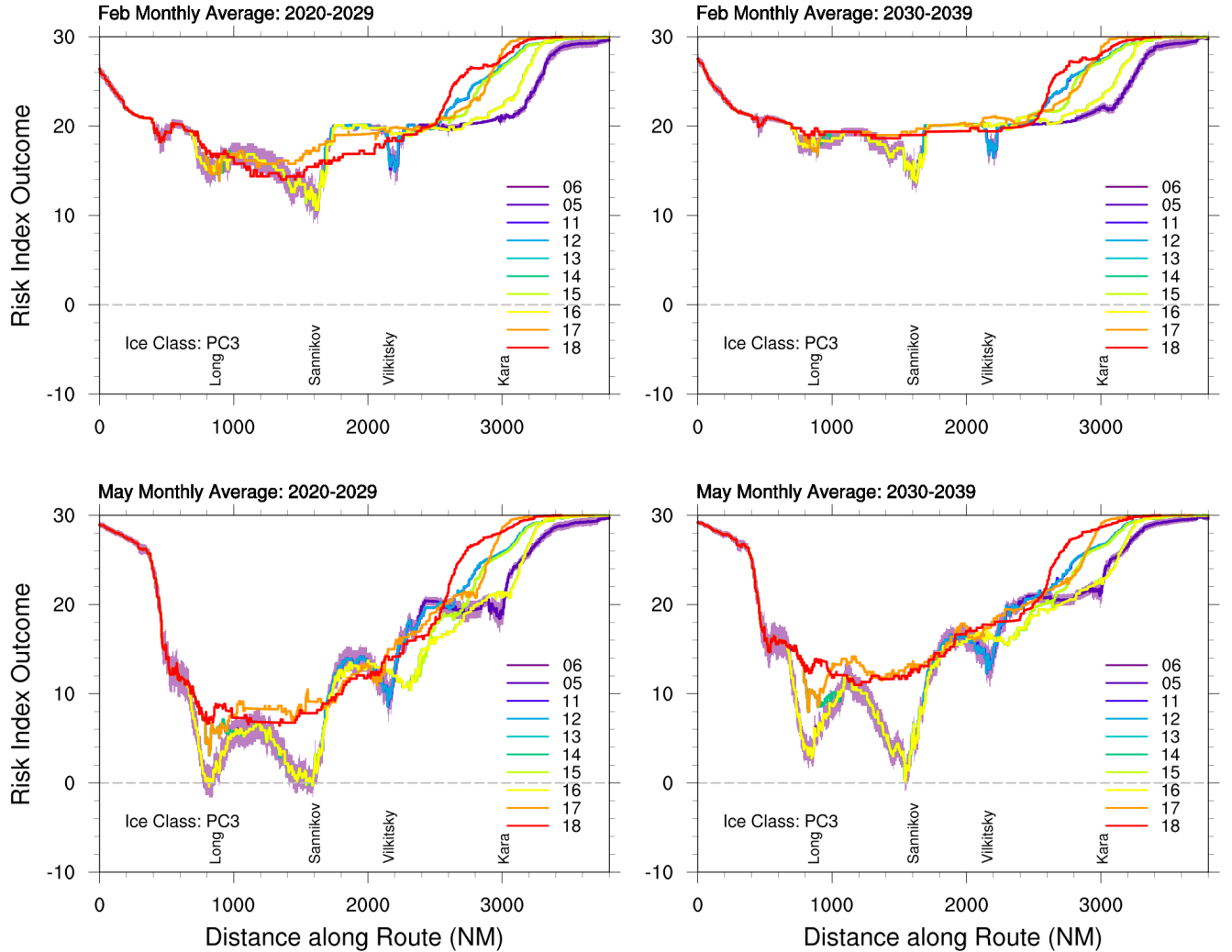


Figure 12: Risk Index Outcome (RIO) along all routes, as numbered, for a Polar Class 3 vessel, also equivalent to an ice class ARC 7. Distances are measured from the Pacific side of the routes. Top/bottom panels represent averages for the months of February and May, respectively, calculated for the decades 2020-2029 (left) and 2030-2039 (right). The shading along route 6 provides the standard error of mean on the RIO calculation. All models in Table 2 are included. The position of the four straits also refers to route 6, which crosses all of them.

Conventional, non-ice-strengthened ships in the IMO classification, would encounter negative RIOs, incurring in “operations subject to special consideration” (and advised to not proceed or seek alternate routes) in December through June during the decade 2050-2059 (Figure 16). However, these vessels could navigate under normal operations in the months August through October already in the decade 2020-2029, and July through November by 2050-2059 (possibly requiring an escort for a small portion of the route in July, or alternatively by avoiding the area of Sannikov Strait, as can be seen in bottom-right panel of Figure 17).

4.7 Limitations of this analysis

There are a number of constraints that must be placed on the interpretation of these results. First, there are limits to the usefulness of multi-model ensembles. While we have selected models based on their ability to reproduce sea ice extent and ocean heat characteristics in the satellite era, this is no guarantee that

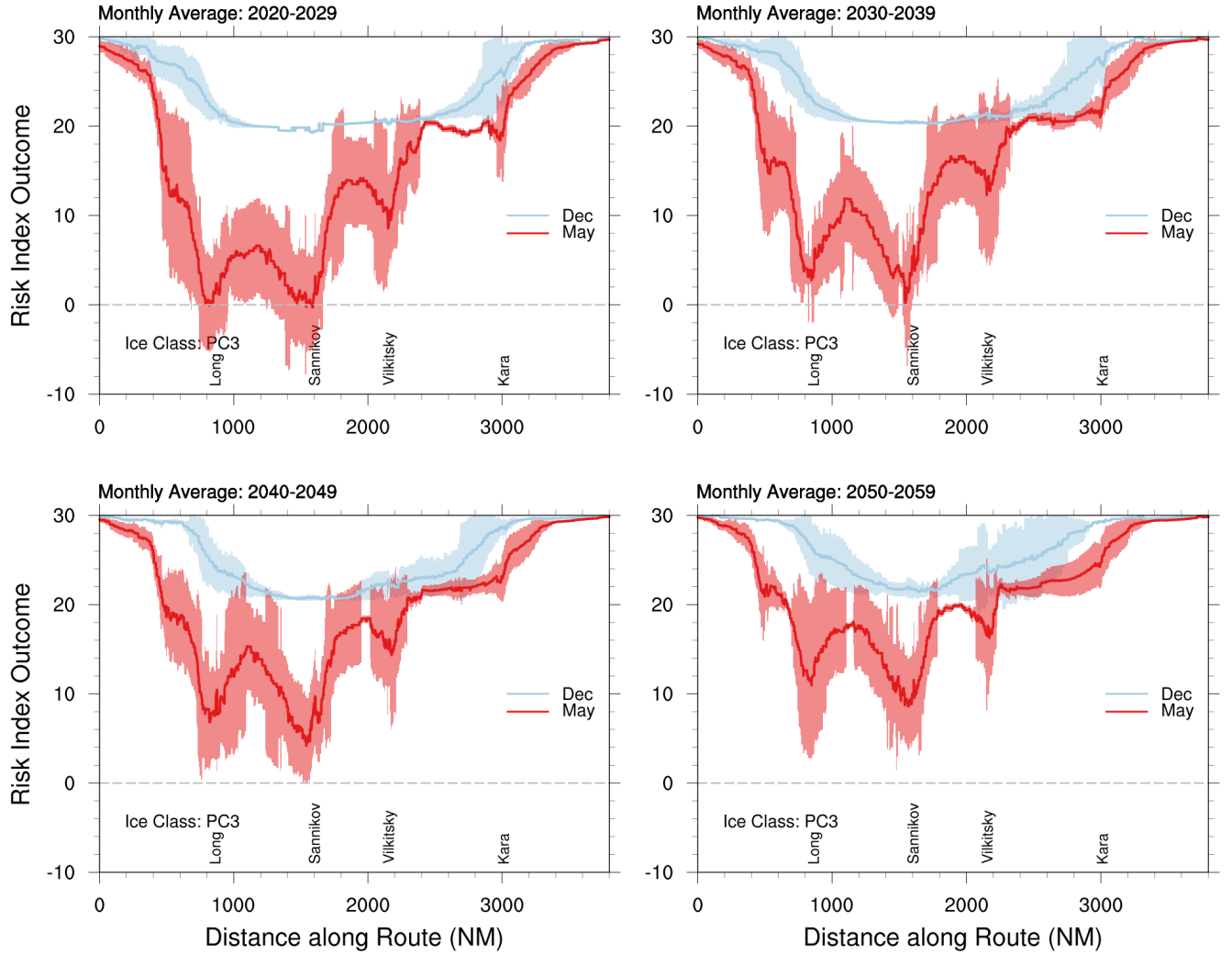


Figure 13: Risk Index Outcome (RIO) along route 6, for a Polar Class 3 vessel, also equivalent to an ice class ARC 7. Distances are measured from the Pacific side of the route. The lines represent the RIO assessment obtained as mean of the distribution of model values at each route point. The shading covers the 50% probability of the distribution of model values, estimated by the “interquartile” range. Different colors indicate the outcome for the months December and May, calculated for four different decades, as indicated. All models in Table 2 are included. The position of the four straits along the route are also marked.

each model’s physics is appropriate for future climate change. The present-day performance, however, is the best indication available of a model’s ability to reproduce key aspects of Arctic climate. Nonetheless, there remains considerable spread in predictions of the first ice-free September in the Arctic both in our model selection following *Docquier and Koenigk* (2021) and in the broader CMIP6 ensemble (*Notz and Community*, 2020), and we have not presented an error analysis associated with that spread. We also offer the caveat that there is a history of CMIP multi-model ensembles underestimating the pace of climate change in the Arctic (*Hawkins and Sutton*, 2009).

There remains a practical limitation of multi-model ensembles in that all models provide monthly averaged sea ice thickness and concentration, but only select models make daily output accessible and are able to provide distributions of ice thickness within individual grid cells. The analysis method we have adopted necessarily limits the utility of more temporally-resolute model output and more sophisticated models, and

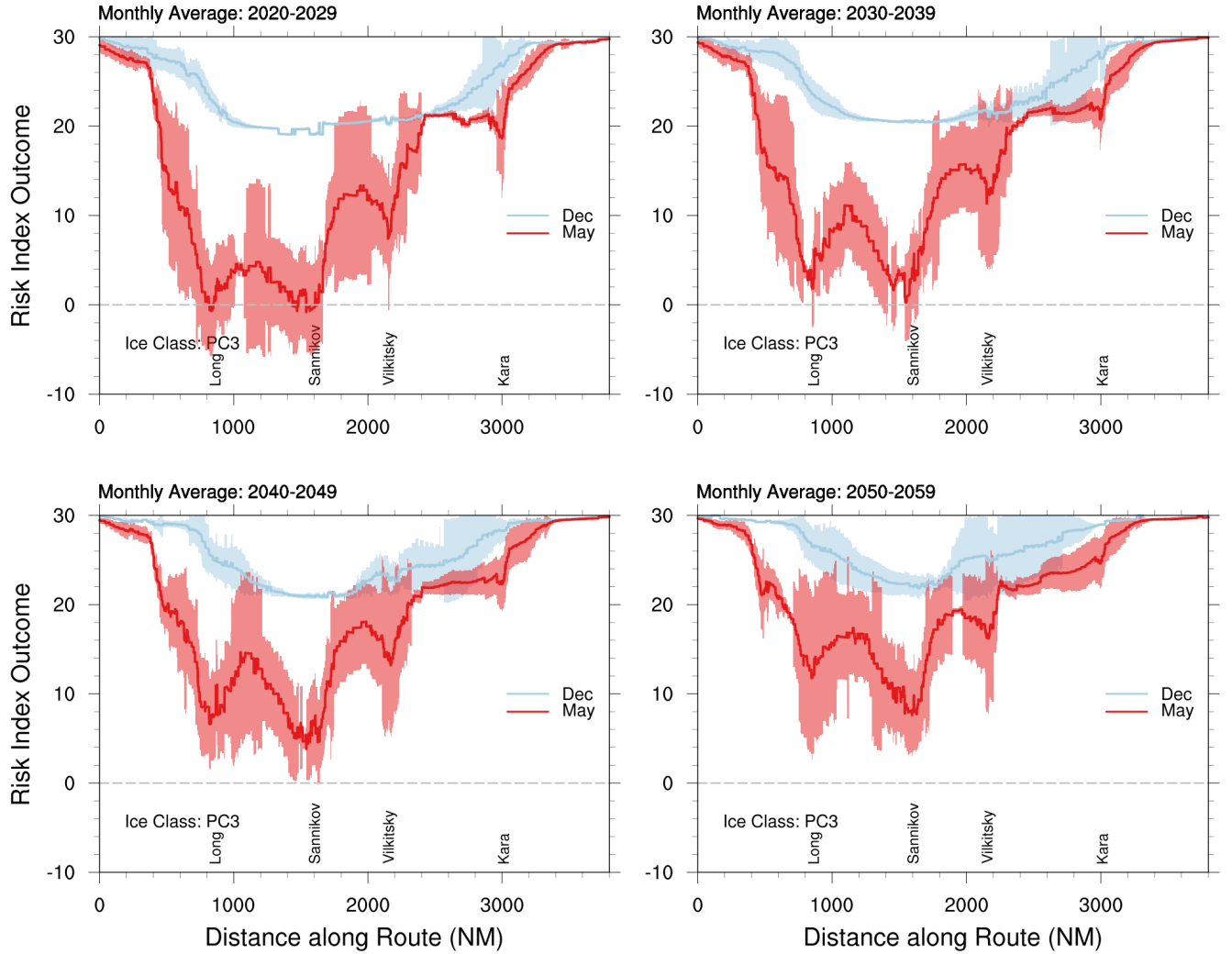


Figure 14: Risk Index Outcome (RIO) along route 6 as in Figure 13, but for the sub-set of models in Table 2 that excludes those in which the route is blocked by land cells.

balances them against an equal weighting of all models across the ensemble. That approach precludes calculating detailed statistics such as “ice free days” along ship routes, because our minimum common averaged time window amongst the models is one month. Our method also precludes weighting models according to their sophistication, including, for example, their ability to mimic observed landfast ice (Figure 18) that is anchored in shallow water and to coasts, and is governed by different physics from the shifting pack. Landfast ice can be as thick as 2 m or more, and the timing of its breakout from coastal regions is a significant navigational consideration (*Meyer et al.*, 2011).

The RIO method of scoring navigability is well suited to the multi-model ensemble approach as we have used it, but is limited in its sophistication because it assigns a single mean ice thickness within each model grid cell, and does not account for sea ice dynamics. As a consequence, sea ice drift speed and direction is negated, even though sea ice velocity at the height of the most risky March-May RIO navigability window directly opposes ship passage toward the Pacific through the East Siberian Sea. Figure 19 illustrates the climatological drift pattern in the central Arctic from 1990 to 2009, and shows that the strongest opposing sea ice velocity occurs in the April-June window for voyages destined for East Asia along the NSR and

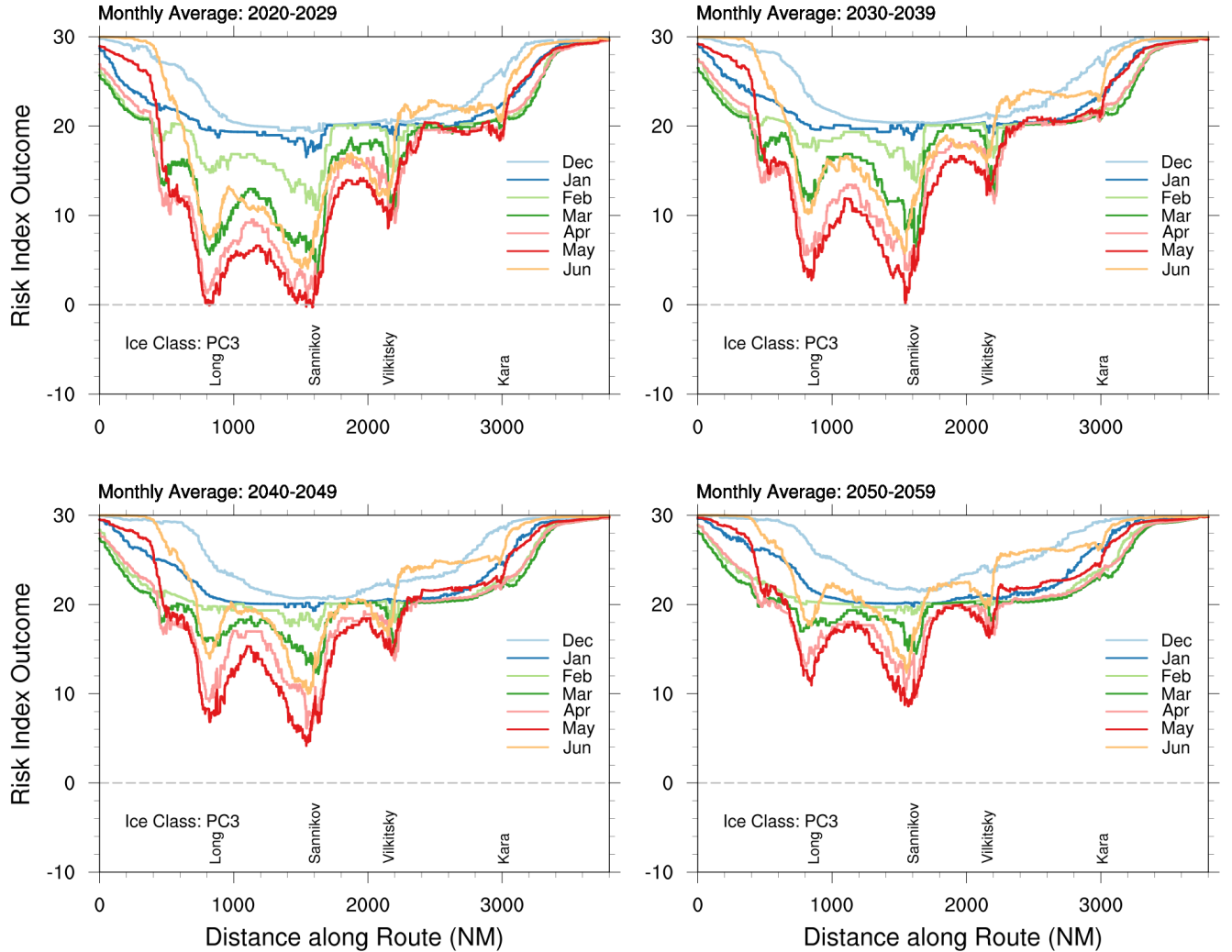


Figure 15: Risk Index Outcome along route 6, for a Polar Class 3 vessel, also equivalent to an ice class ARC 7. Distances are measured from the Pacific side of the route. Different lines indicate results for the months December through June, calculated for four different decades, as indicated. All models in Table 2 are included. The position of the four straits along the route are also marked.

other East Arctic routes.

Finally, we note that broader climatological hazards have not been included in this study pertaining to the coastal support required for Arctic Ocean passage. We have not assessed the long-term risk of sea level rise to coastal liquid natural gas facilities, but note that a recent study suggests that high-north coasts are likely to be subject to less extreme sea level events than in lower-latitudes in the next fifty years (*Tebaldi et al.*, 2021b). Nautical hazards associated with changing tides are not available at present, but are a factor to be considered in shallow straits, especially for the passage of large ships through Sannikov Strait, which has among the largest tidal amplitudes on the NSR, and may be susceptible to changes in tidal amplitudes and phases with an increasingly-seasonal ice coverage (e.g. *Kagan and Sofina*, 2010). We have also not included an assessment of the risk of increasing wave heights in the Arctic Ocean and to coastlines as a result of decreasing sea ice cover (e.g. *Waseda et al.*, 2018). But we point out that fetch limiting dictates that highly destructive long-period waves may be uncommon in an ice-free central Arctic. However, short-period, steep

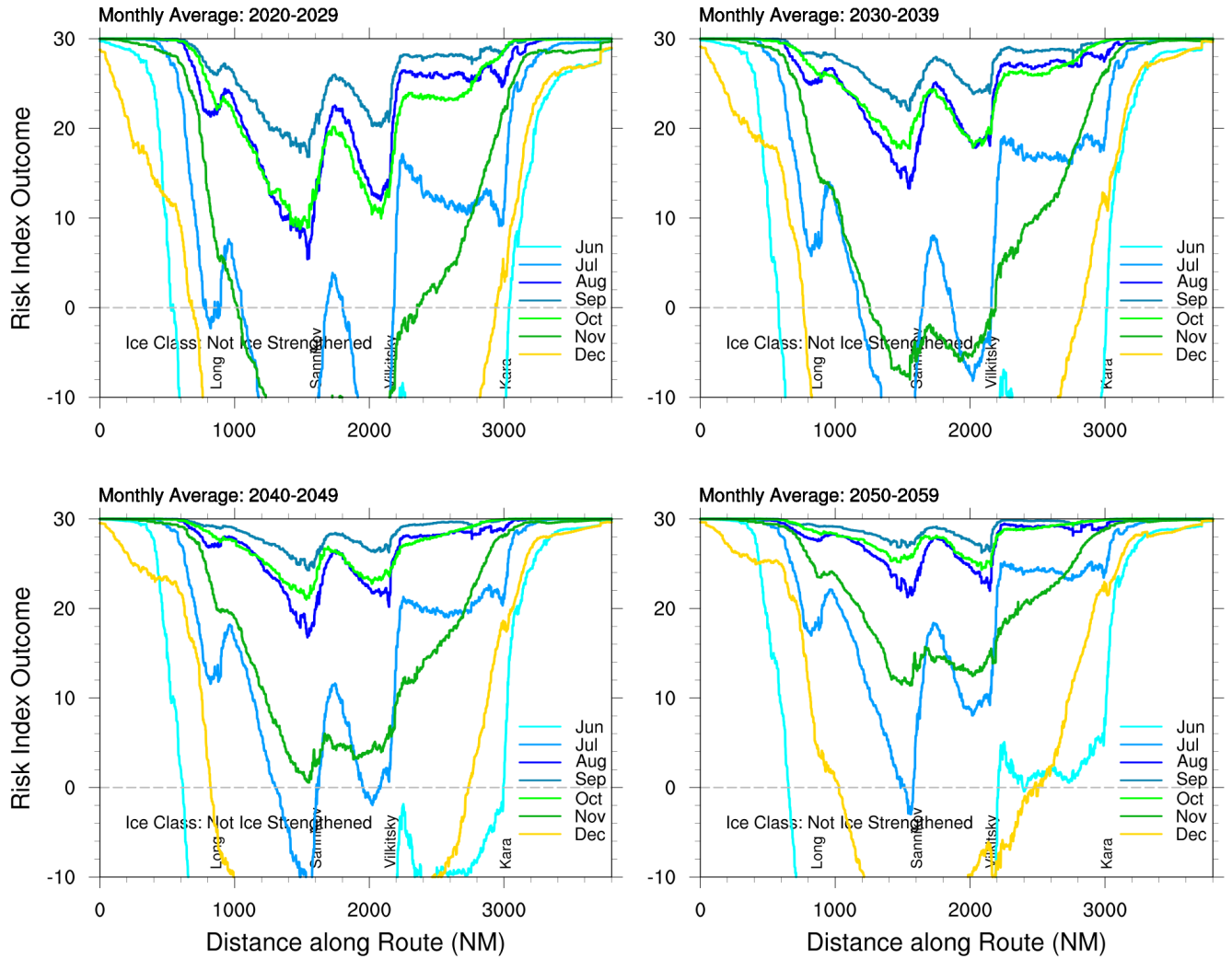


Figure 16: Risk Index Outcome along route 6, for a conventional, non-ice-strengthened vessel. Distances are measured from the Pacific side of the route. Different lines indicate results for the months June through December, calculated for four different decades, as indicated. All models in Table 2 are included. The position of the four straits along the route are also marked.

waves may occur in shallow water without future attenuation by sea ice, which may unduly affect navigation through straits we have identified as having the highest navigational risk. Finally, the impact of thawing permafrost on land-based shipping infrastructure has not been assessed.

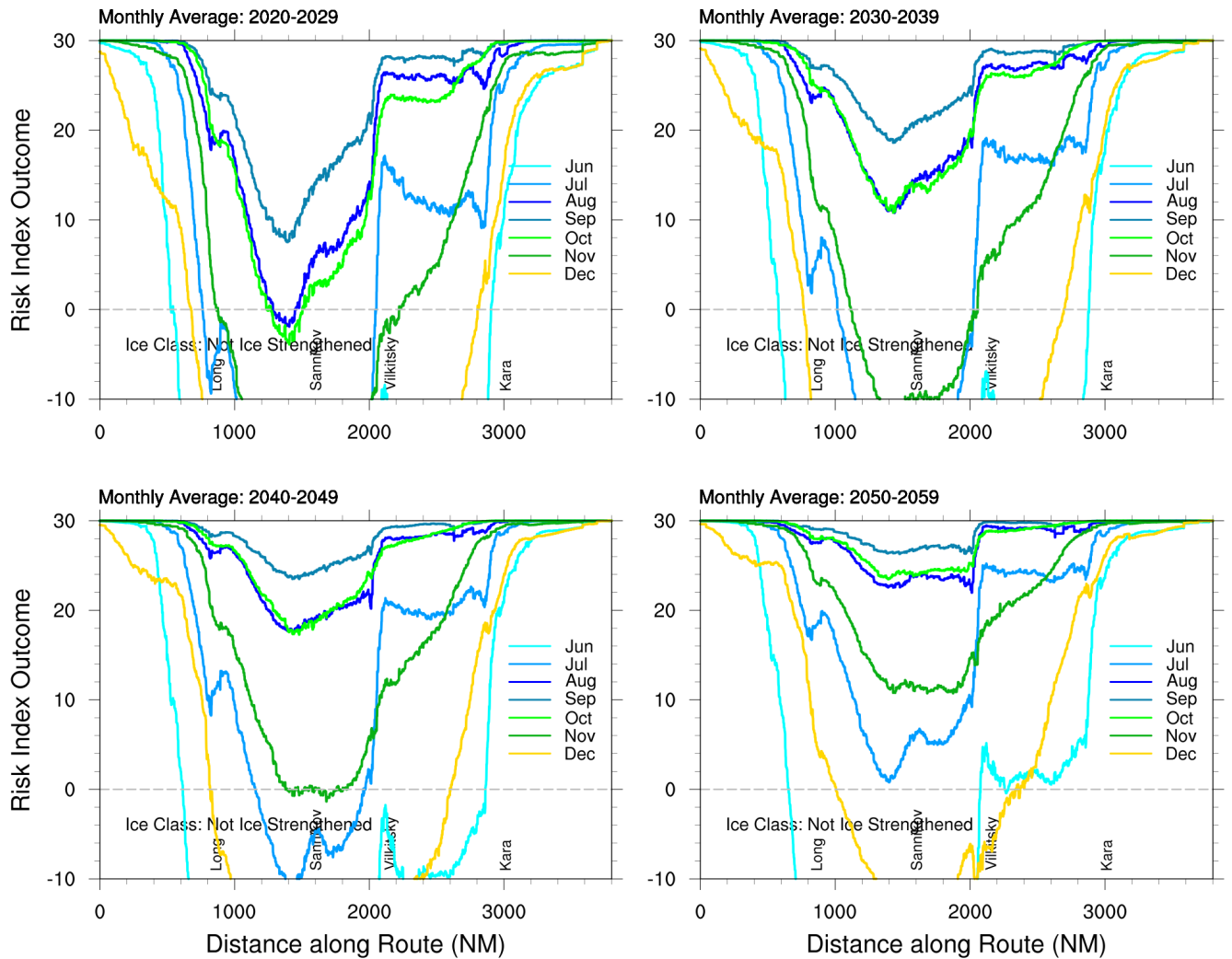


Figure 17: As Figure 16 but for RIOs estimated along route 20 (which passes northward of Sannikov Strait), for a conventional, non-ice-strengthened vessel. Distances are measured from the Pacific side of the route. All models in Table 2 are included. Note that the distances of the four straits refer to the coastal route 6.

References

- Armour, K. C., I. Eisenman, E. Blanchard-Wrigglesworth, K. E. McCusker, and C. M. Bitz (2011), The reversibility of sea ice loss in a state-of-the-art climate model, *Geophysical Research Letters*, *38*(16), 1–5, doi:10.1029/2011GL048739.
- Dai, A., D. Luo, M. Song, and J. Liu (2019), Arctic amplification is caused by sea-ice loss under increasing CO₂, *Nature Communications*, *10*(1), 121, doi:10.1038/s41467-018-07954-9.
- Davy, R., and S. Outten (2020), The arctic surface climate in CMIP6: Status and developments since CMIP5, *Journal of Climate*, *33*(18), 8047–8068, doi:10.1175/JCLI-D-19-0990.1.
- Davy, R., L. Chen, and E. Hanna (2018), Arctic amplification metrics, *International Journal of Climatology*, *38*(12), 4384–4394, doi:10.1002/joc.5675.

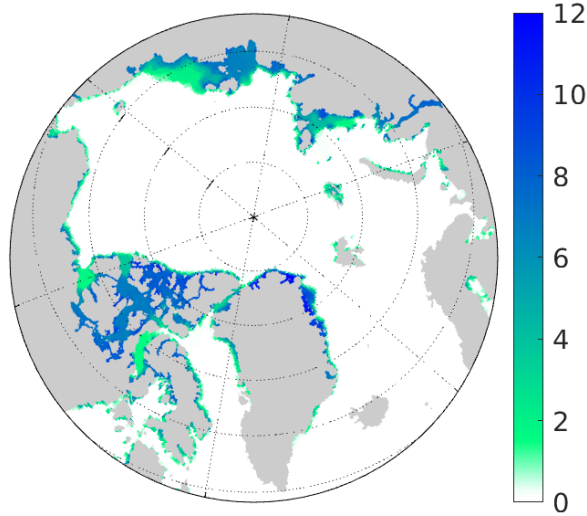


Figure 18: Average number of months of landfast ice in the Arctic, per year, for September 2004 - September 2007 from observations (Fetterer and Fowley, 2006, updated 2009). Figure courtesy J.-F. Lemieux, ECCC.

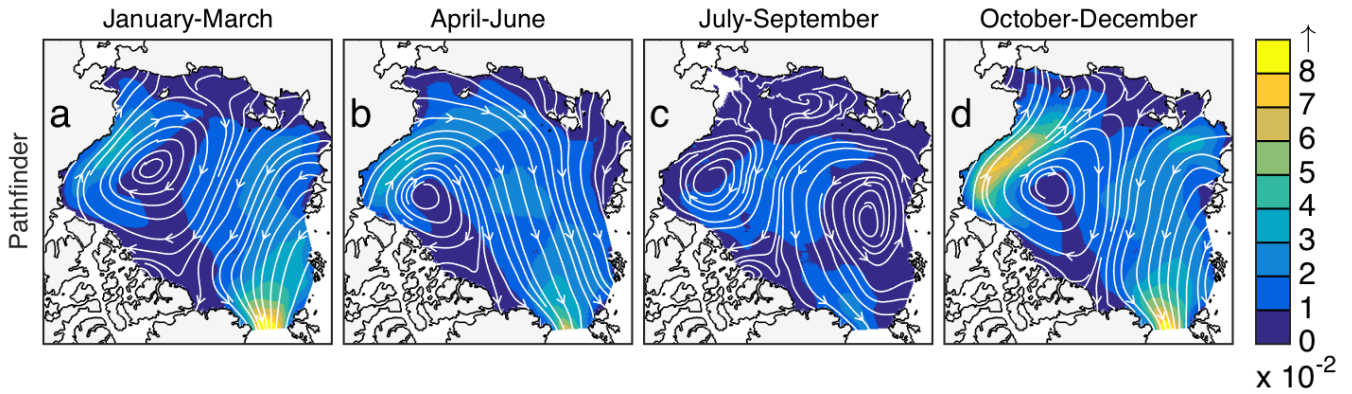


Figure 19: Average 1990-2009 three-monthly sea ice streamlines and drift speed (color shading; m s^{-1}) according to Pathfinder sea ice drift derived from satellite and in *in-situ* buoy observations (Tschudi *et al.*, 2016). In each panel, the Canadian Archipelago is situated on the lower left corner, Alaska in the upper left, and Russia along the top and upper right.

Docquier, D., and T. Koenigk (2021), Observation-based selection of climate models projects arctic ice-free summers around 2035, *Communications Earth & Environment*, 2(1), 144, doi:10.1038/s43247-021-00214-7.

Eisenman, I., and J. S. Wettlaufer (2009), Nonlinear threshold behavior during the loss of Arctic sea ice, *Proceedings of the National Academy of Sciences of the United States of America*, 106(1), 28–32, doi: Doi10.1073/Pnas.0806887106.

Eyring, V., S. Bony, G. A. Meehl, C. A. Senior, B. Stevens, R. J. Stouffer, and K. E. Taylor (2016), Overview of the Coupled Model Intercomparison Project Phase 6 (CMIP6) experimental design and organization, *Geoscientific Model Development*, 9(5), 1937–1958, doi:10.5194/gmd-9-1937-2016.

Fetterer, F., and C. Fowley (2006, updated 2009), National Ice Center Arctic Sea Ice Charts and Climatologies in Gridded Format, *Tech. rep.*, National Snow and Ice Data Center, Boulder, CO, digital media.

Hawkins, E., and R. Sutton (2009), The Potential to Narrow Uncertainty in Regional Climate Predictions, *Bull. Am. Meteorol. Soc.*, 90(8), 1095–1107, doi:10.1175/2009bams2607.1.

- he Liu, X., L. Ma, J. yue Wang, Y. Wang, and L. na Wang (2017), Navigable windows of the Northwest Passage, *Polar Science*, *13*, 91–99, doi:10.1016/j.polar.2017.02.001.
- International Maritime Organization (2002), Guidelines for Ships Operating in Arctic Ice-Covered Waters, *Tech. rep.*, International Maritime Organization, London.
- Jahn, A., and M. M. Holland (2013), Implications of Arctic sea ice changes for North Atlantic deep convection and the meridional overturning circulation in CCSM4-CMIP5 simulations, *Geophysical Research Letters*, *40*(6), 1206–1211, doi:10.1002/grl.50183.
- Johannessen, O. M., L. Bengtsson, M. W. Miles, S. I. Kuzmina, V. A. Semenov, G. V. Alekseev, A. P. Nagurnyi, V. F. Zakharov, L. P. Bobylev, L. H. Pettersson, K. Hasselmann, and H. P. Cattle (2004), Arctic climate change: observed and modelled temperature and sea-ice variability, *Tellus A: Dynamic Meteorology and Oceanography*, *56*(4), 328–341, doi:10.3402/tellusa.v56i4.14418.
- Kagan, B. A., and E. V. Sofina (2010), Ice-induced seasonal variability of tidal constants in the Arctic Ocean, *Cont. Shelf Res.*, *30*(6), 643–647, doi:10.1016/j.csr.2009.05.010.
- Meyer, F. J., A. R. Mahoney, H. Eiken, C. L. Denny, H. C. Druckenmiller, and S. Hendricks (2011), Mapping arctic landfast ice extent using L-band synthetic aperture radar interferometry, *Remote Sens. Environ.*, *115*(12), 3029–3043, doi:10.1016/J.RSE.2011.06.006.
- Muntjewerf, L., M. Petrini, M. Vizcaino, C. Ernani da Silva, R. Sellevold, M. D. Scherrenberg, K. Thayer-Calder, S. L. Bradley, J. T. Lenaerts, W. H. Lipscomb, and M. Lofverstrom (2020), Greenland Ice Sheet Contribution to 21st Century Sea Level Rise as Simulated by the Coupled CESM2.1-CISM2.1, *Geophysical Research Letters*, *47*(9), doi:10.1029/2019GL086836.
- Notz, D., and S. Community (2020), Arctic Sea Ice in CMIP6, *Geophysical Research Letters*, *47*(10), doi:10.1029/2019GL086749.
- Notz, D., and J. Stroeve (2016), Observed Arctic sea-ice loss directly follows anthropogenic CO2 emission, *Science*, *354*(6313), doi:10.1126/science.aag2345.
- Pastusiak, T. (2016), *The northern sea route as a shipping lane: Expectations and reality*, 1–219 pp., doi:10.1007/978-3-319-41834-6.
- Perovich, D. K., J. A. Richter-Menge, K. F. Jones, and B. Light (2008), Sunlight, water, and ice: Extreme Arctic sea ice melt during the summer of 2007, *Geophysical Research Letters*, *35*(11), –, doi:ArtnL11501Doi10.1029/2008gl034007.
- Riahi, K., D. P. van Vuuren, E. Kriegler, J. Edmonds, B. C. O’Neill, S. Fujimori, N. Bauer, K. Calvin, R. Dellink, O. Fricko, W. Lutz, A. Popp, J. C. Cuaresma, S. KC, M. Leimbach, L. Jiang, T. Kram, S. Rao, J. Emmerling, K. Ebi, T. Hasegawa, P. Havlik, F. Humpenöder, L. A. Da Silva, S. Smith, E. Stehfest, V. Bosetti, J. Eom, D. Gernaat, T. Masui, J. Rogelj, J. Streffer, L. Drouet, V. Krey, G. Luderer, M. Harmesen, K. Takahashi, L. Baumstark, J. C. Doelman, M. Kainuma, Z. Klimont, G. Marangoni, H. Lotze-Campen, M. Obersteiner, A. Tabeau, and M. Tavoni (2017), The Shared Socioeconomic Pathways and their energy, land use, and greenhouse gas emissions implications: An overview, *Global Environmental Change*, *42*, 153–168, doi:10.1016/j.gloenvcha.2016.05.009.
- Slingo, J., and T. Palmer (2011), Uncertainty in weather and climate prediction, *Philosophical Transactions of the Royal Society A: Mathematical, Physical and Engineering Sciences*, *369*(1956), 4751–4767, doi:doi.org/10.1098/rsta.2011.0161.
- Steele, M., J. Zhang, and W. Ermold (2010), Mechanisms of summertime upper Arctic Ocean warming and the effect on sea ice melt, *Journal of Geophysical Research*, *115*(C11), C11,004, doi:10.1029/2009JC005849.

- Stuecker, M. F., C. M. Bitz, K. C. Armour, C. Proistosescu, S. M. Kang, S. P. Xie, D. Kim, S. McGregor, W. Zhang, S. Zhao, W. Cai, Y. Dong, and F. F. Jin (2018), Polar amplification dominated by local forcing and feedbacks, *Nature Climate Change*, 8(12), 1076–1081, doi:10.1038/s41558-018-0339-y.
- Tebaldi, C., K. Debeire, V. Eyring, E. Fischer, J. Fyfe, P. Friedlingstein, R. Knutti, J. Lowe, B. O’Neill, B. Sanderson, D. Van Vuuren, K. Riahi, M. Meinshausen, Z. Nicholls, K. Tokarska, G. Hurtt, E. Kriegler, G. Meehl, R. Moss, S. Bauer, O. Boucher, V. Brovkin, Y. Yhb, M. Dix, S. Gualdi, H. Guo, J. John, S. Kharin, Y. H. Kim, T. Koshiro, L. Ma, D. Olivié, S. Panickal, F. Qiao, X. Rong, N. Rosenbloom, M. Schupfner, R. Séférian, A. Sellar, T. Semmler, X. Shi, Z. Song, C. Steger, R. Stouffer, N. Swart, K. Tachiiri, Q. Tang, H. Tatebe, A. Voldoire, E. Volodin, K. Wyser, X. Xin, S. Yang, Y. Yu, and T. Ziehn (2021a), Climate model projections from the Scenario Model Intercomparison Project (ScenarioMIP) of CMIP6, *Earth System Dynamics*, 12(1), 253–293, doi:10.5194/esd-12-253-2021.
- Tebaldi, C., R. Ranasinghe, M. Vourdoukas, D. J. Rasmussen, B. Vega-Westhoff, E. Kirezci, R. E. Kopp, R. Sriver, and L. Mentaschi (2021b), Extreme sea levels at different global warming levels, *Nature Climate Change*, 11(9), 746–751, doi:10.1038/s41558-021-01127-1.
- Tschudi, M., C. Fowler, J. Maslanik, J. S. Stewart, and W. Meier (2016), *Polar Pathfinder Daily 25 km EASE-Grid Sea Ice Motion Vectors, Version 3*, Digital Media, NASA National Snow and Ice Data Center Distributed Active Archive Center, Boulder, Colorado, USA., doi:10.5067/O57VAIT2AYYY.
- Waseda, T., A. Webb, K. Sato, J. Inoue, A. Kohout, B. Penrose, and S. Penrose (2018), Correlated Increase of High Ocean Waves and Winds in the Ice-Free Waters of the Arctic Ocean, *Sci. Rep.*, 8(1), 1–9, doi:10.1038/s41598-018-22500-9.
- Wei, T., Q. Yan, W. Qi, M. Ding, and C. Wang (2020), Projections of Arctic sea ice conditions and shipping routes in the twenty-first century using CMIP6 forcing scenarios, *Environmental Research Letters*, 15(10), doi:10.1088/1748-9326/abb2c8.

Appendix A Sea Ice Concentration along Routes

Additional sea ice concentration plots not shown in the main text are reported here. Figures 20 through 22 illustrate the concentration of sea ice along all ship routes (distances are measured from the Bering Strait to the Atlantic ocean), calculated from the models in Table 2. Data cover the months of December through July and September, this last taken as representative of the month with minimum Arctic sea ice coverage. Data are averaged in each of four decades (from top to bottom). The four major straits along the Siberia's North coast are indicated, using distances along route 6, which crosses all of them. Note that the distance of the straits along the various routes is, in general, different.

Appendix B RIO Monthly Assessment along routes 6 and 20

Route 6 crosses all main straits along the North Siberia coast (see Figure 2 and 6). In particular, Sannikov Strait, which separates the Anzhu Islands from the Lyakhovsky Islands, and the Long Strait, south of Wrangel Island, are typically the passages that present the highest risk to ship operations according to the RIO score, as shown in Figure 13. As route 6, route 20 also crosses Vilkitsky and Kara straits, but this route proceeds North of Anzhu Islands, avoiding the Sannikov Strait and the East Siberian Sea which typically pose a high risk to ship operations. Route 20 also avoids Long Straits, passing North of Wrangel Island. Here, in Figures 23 and 24, RIO plots are presented along route 6, averaged in each month, for the four decades of the analysis. Equivalent plots for route 20 are shown in Figures 25 and 26. The Risk Index Outcomes are evaluated for a Polar Class 3 (or ARC 7) ice class vessel. RIO scores are calculated including all models in Table 2. Distances are measured from the Pacific side of the route. In the plots, the RIO is calculated as the mean of the values derived from model variables, at each route point. The dispersion around the mean is characterized by the interquartile range of the distribution, i.e., the difference between the third quartile (75th percentile) and the first quartile (25th percentile) of the distribution of values. From a statistical perspective, this is not an estimate of the error on the mean, which would involve the standard deviation of the sample divided by the number of sample values, but rather a measure of the dispersion of model predictions.

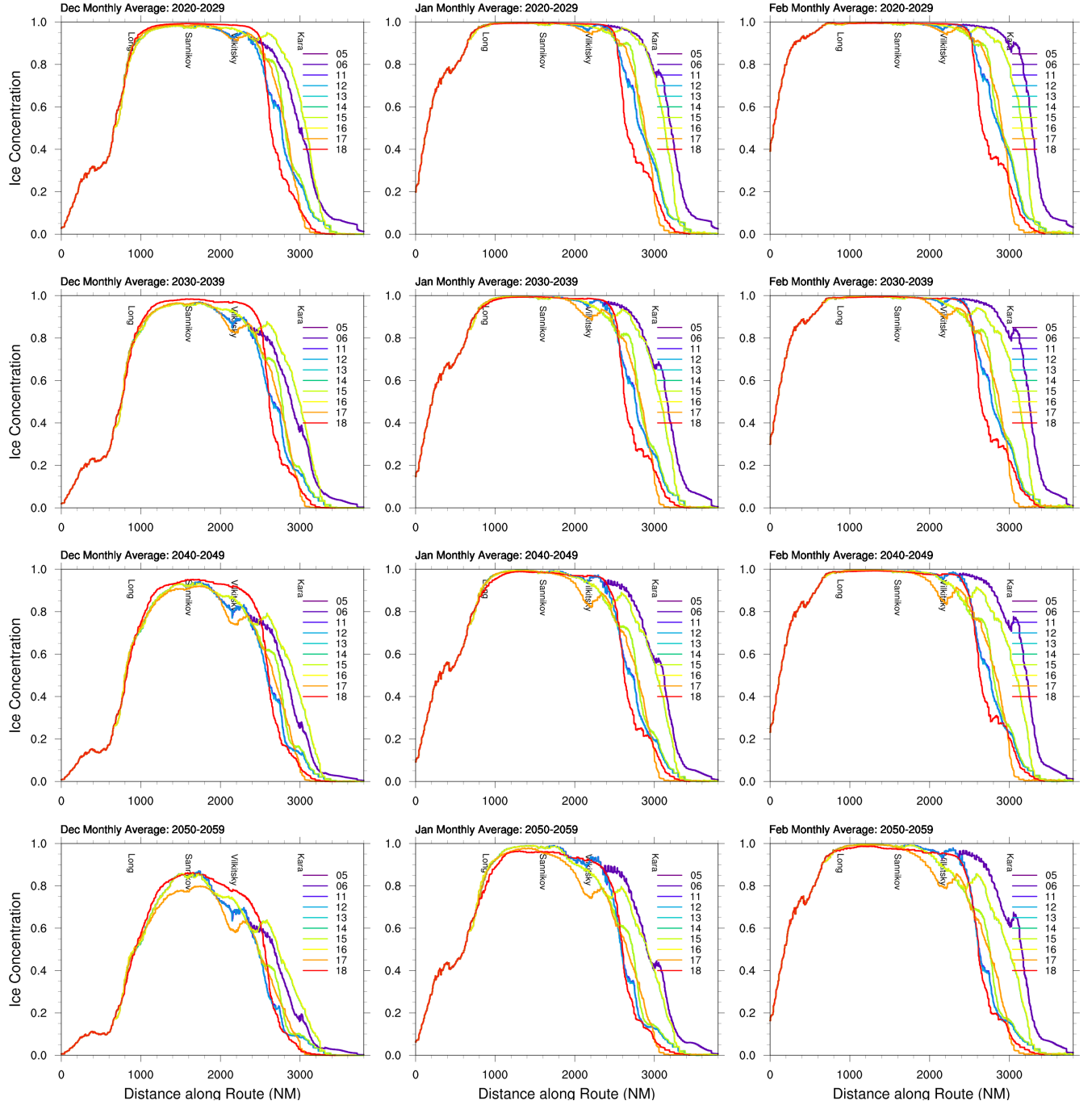


Figure 20: Sea ice concentration along all ship routes (as numbered), from the Bering Strait to the Atlantic ocean. Concentration values represent the mean from all models in Table 2. Data are for the months Dec-Jan-Feb (from left to right), averaged on a decade, as indicated, from top to bottom. The four major straits along the Siberian coast are marked, using distances along route 6, which crosses all of them.

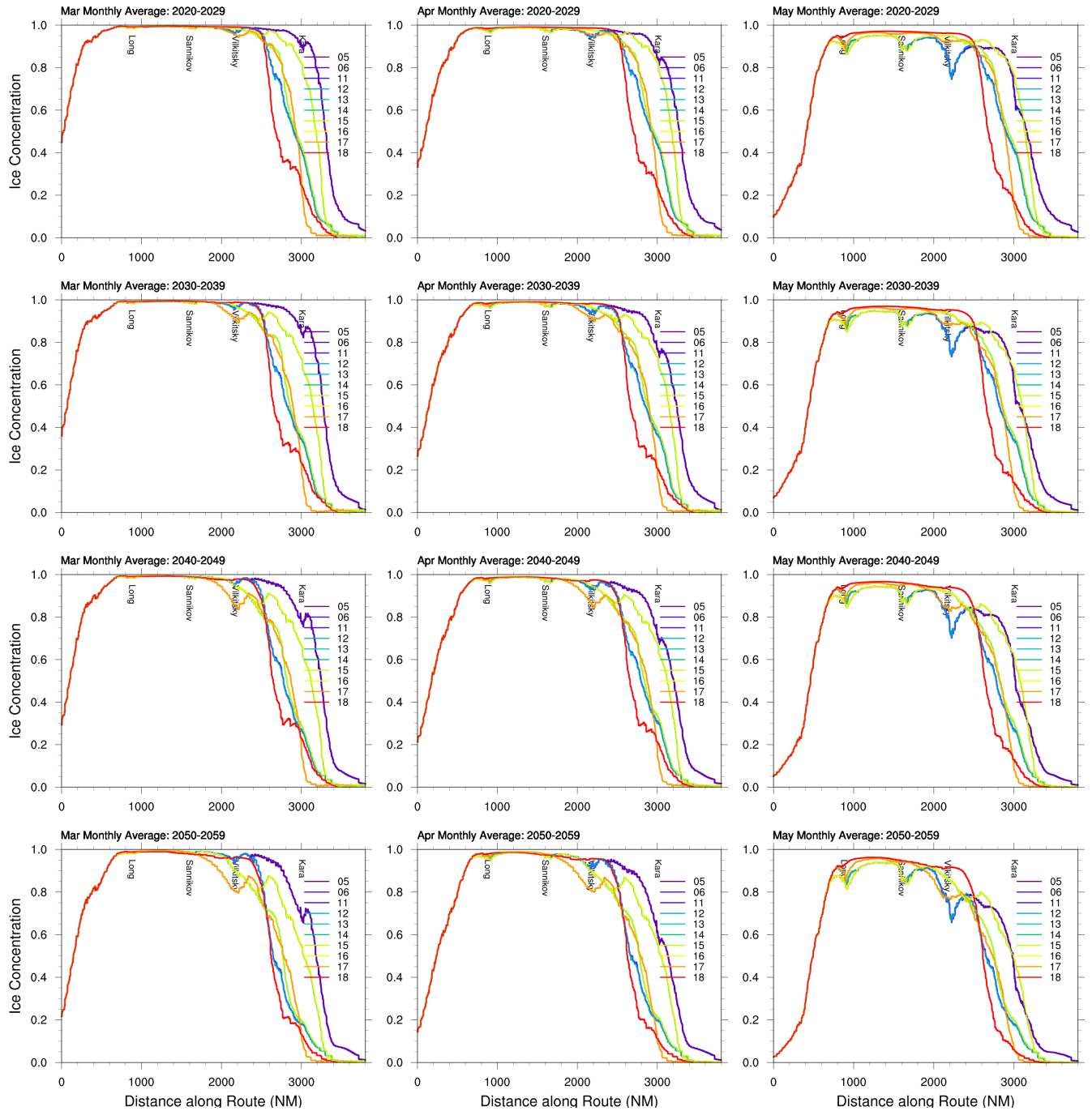


Figure 21: As Figure 20, but for the months of March (left), April (center), and May (right).

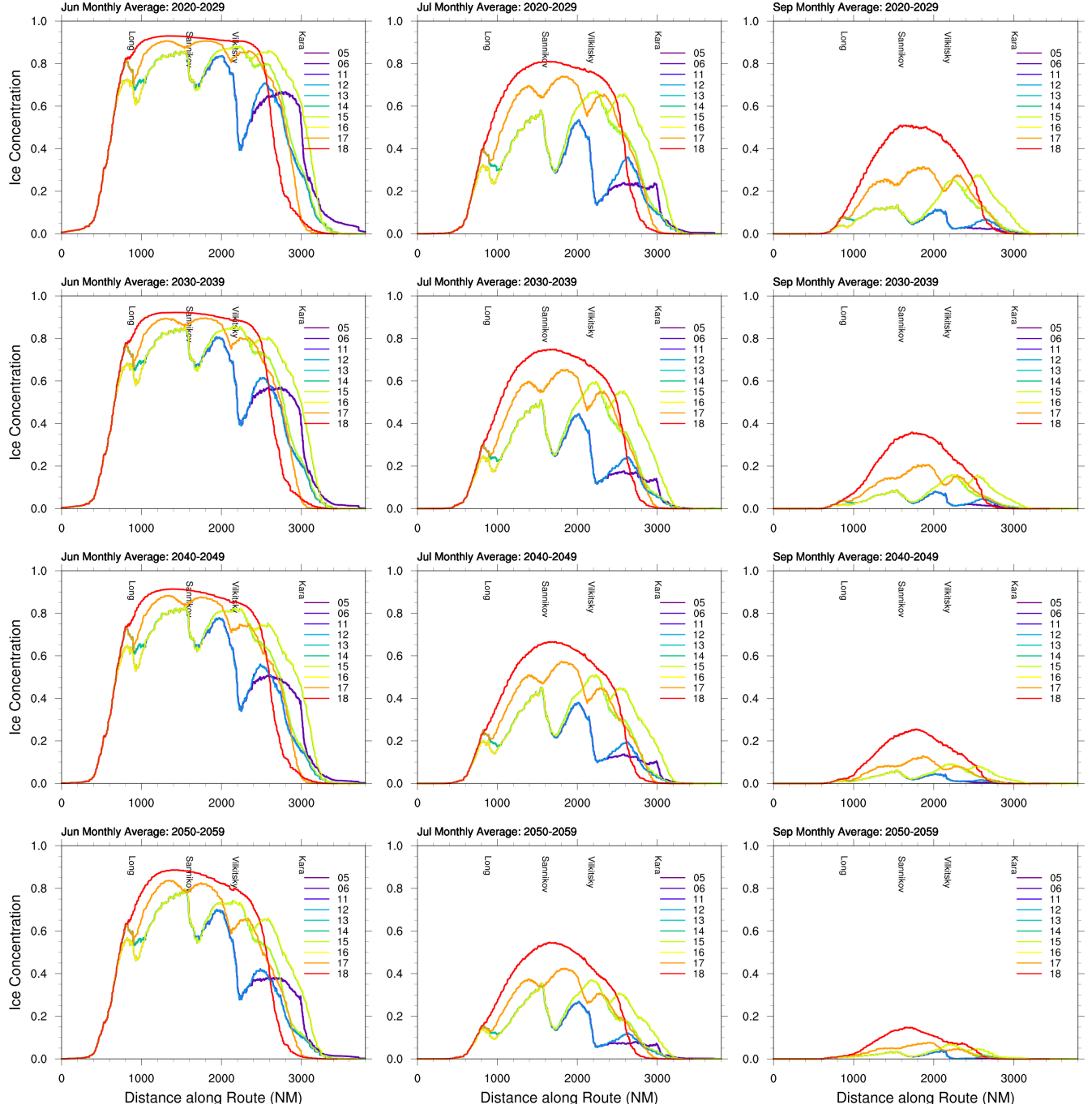


Figure 22: As Figure 20, but for the months of June (left), July (center), and September (right).

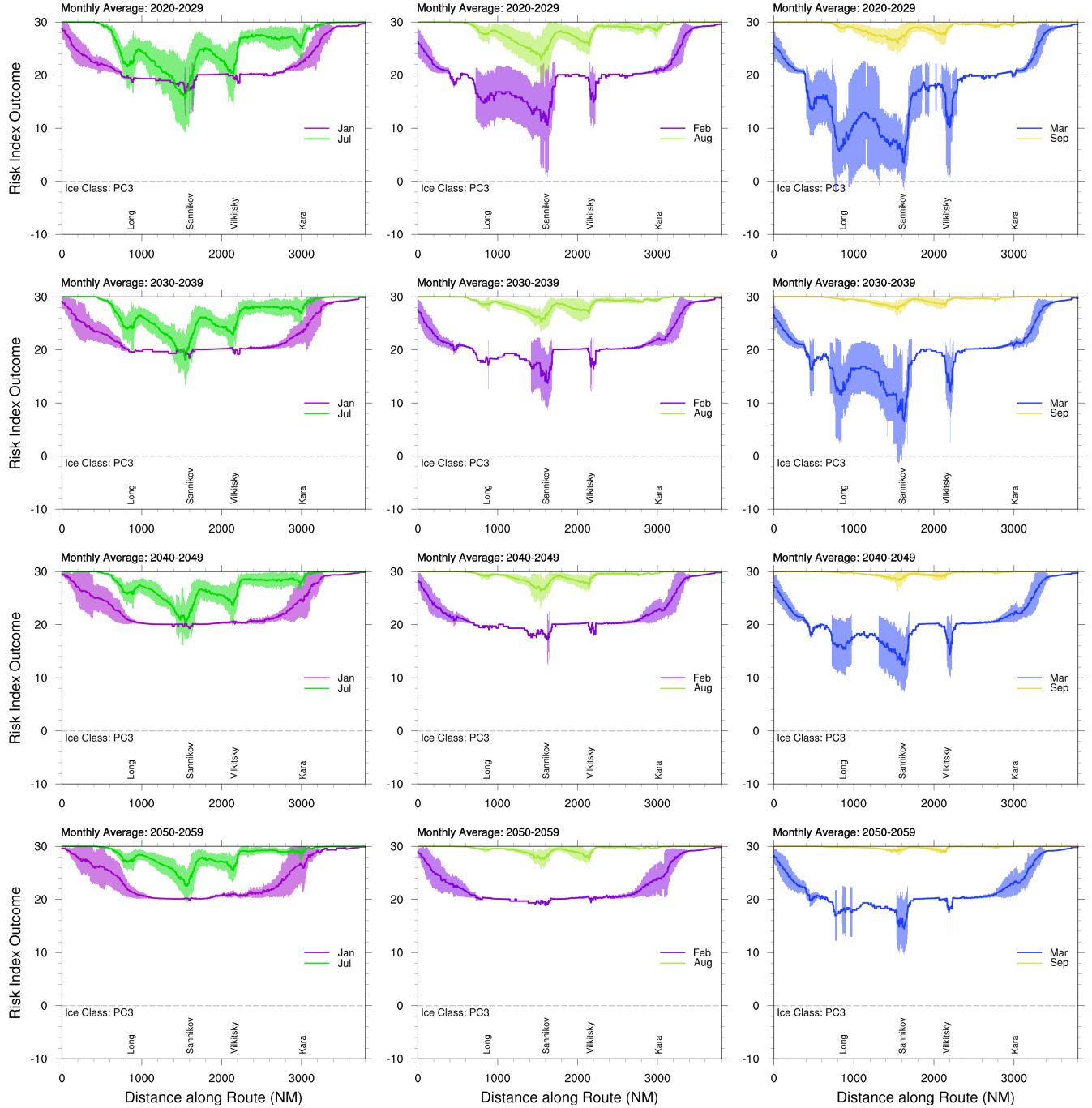


Figure 23: Risk Index Outcome (RIO) along route 6 (see Figure 2 and 6). Distances are measured from the Bering Strait to the Atlantic ocean. RIO values represent the mean from all models in Table 2 at each route point. The four major straits along the Siberian North coast are also marked.

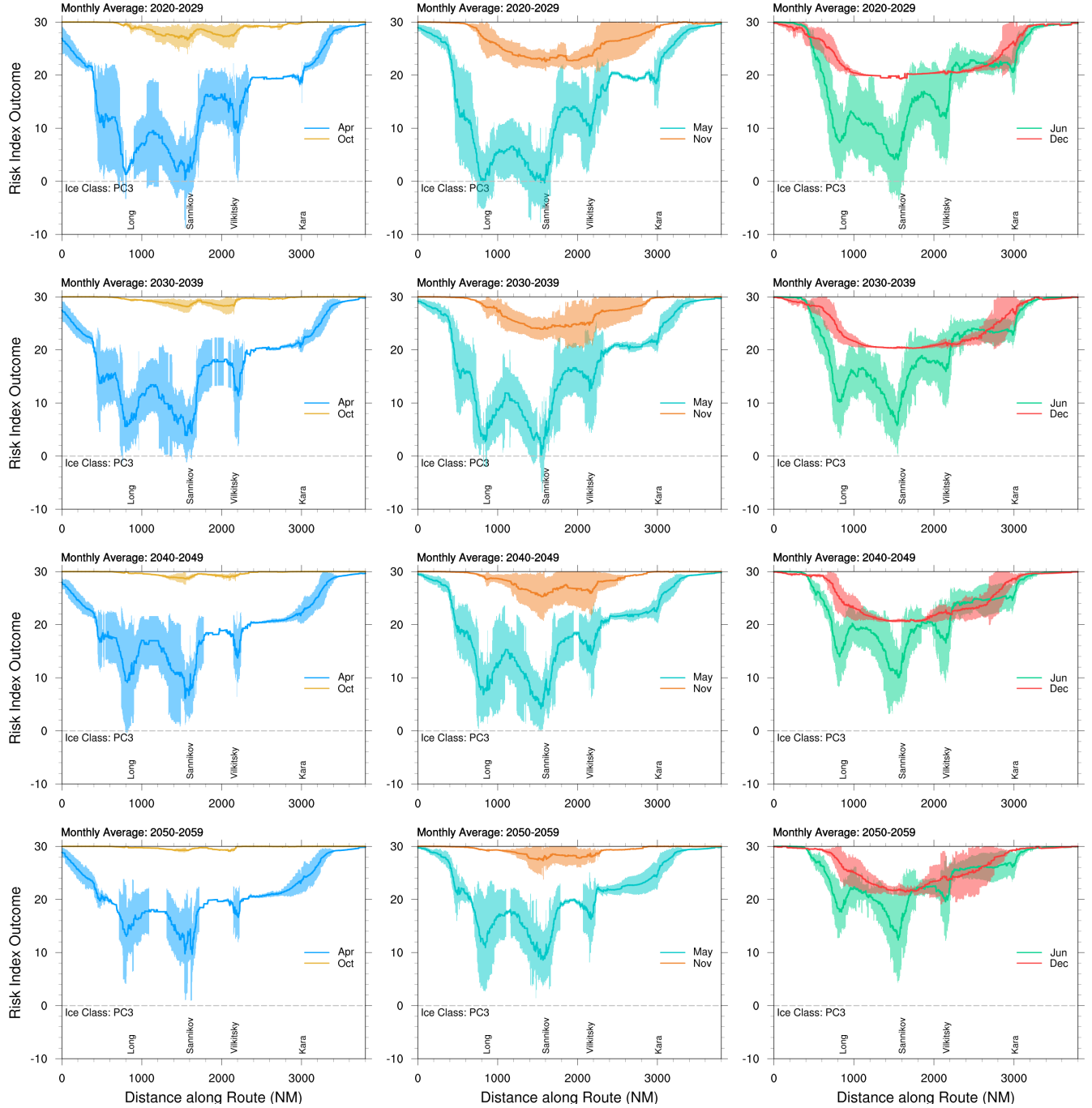


Figure 24: As in Figure 23, but RIOs indicate means and spread along route 6 for different months of the decades 2020–2029 through 2050–2059.

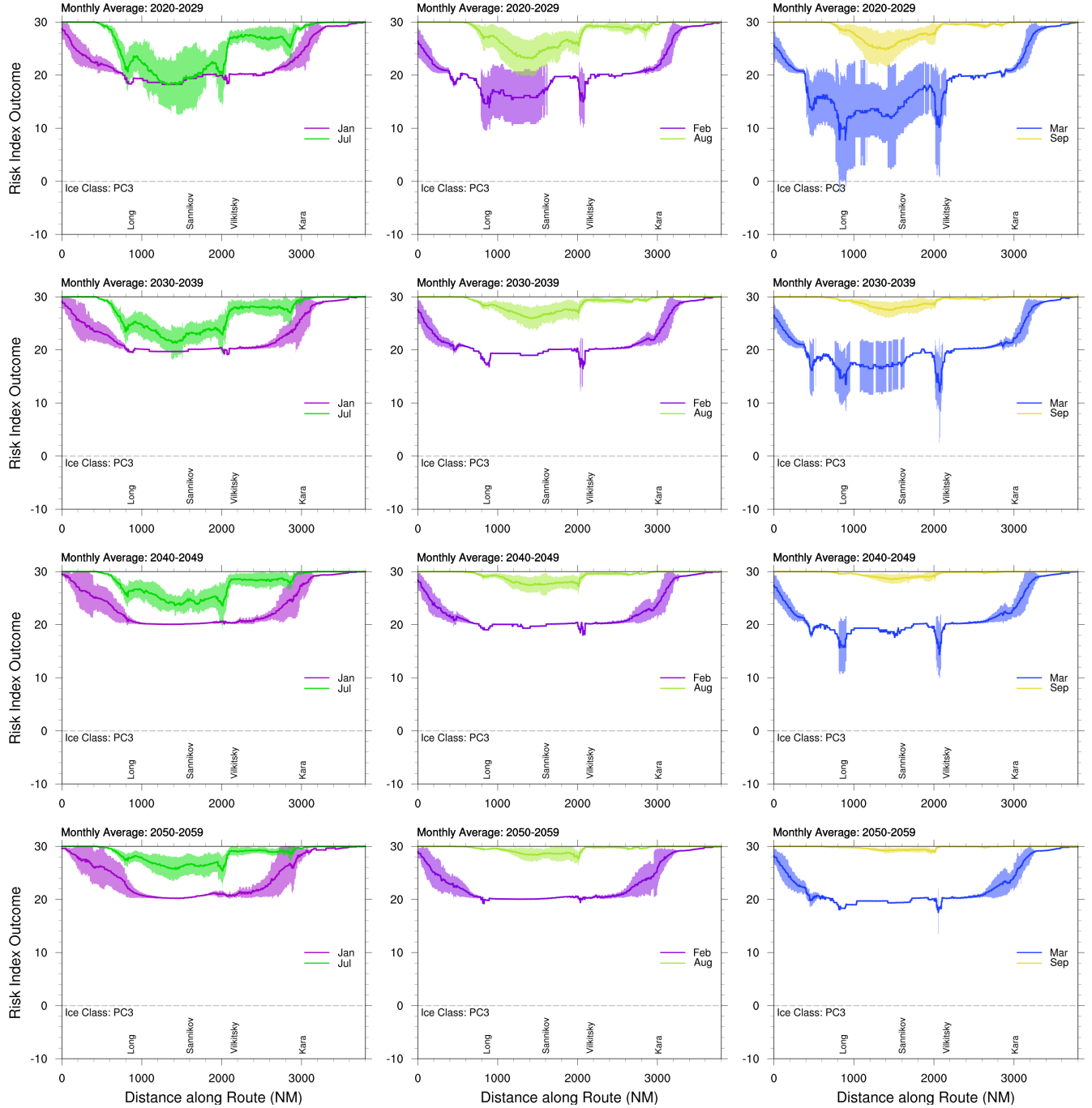


Figure 25: Risk Index Outcome along route 20 (see Figure 2 and 6). Distances are measured from the Bering Strait to the Atlantic ocean. RIO values represent the mean from all models in Table 2 at each route point. The distances of the four straits along the Siberian North coast refer to route 6 and are shown as a references.

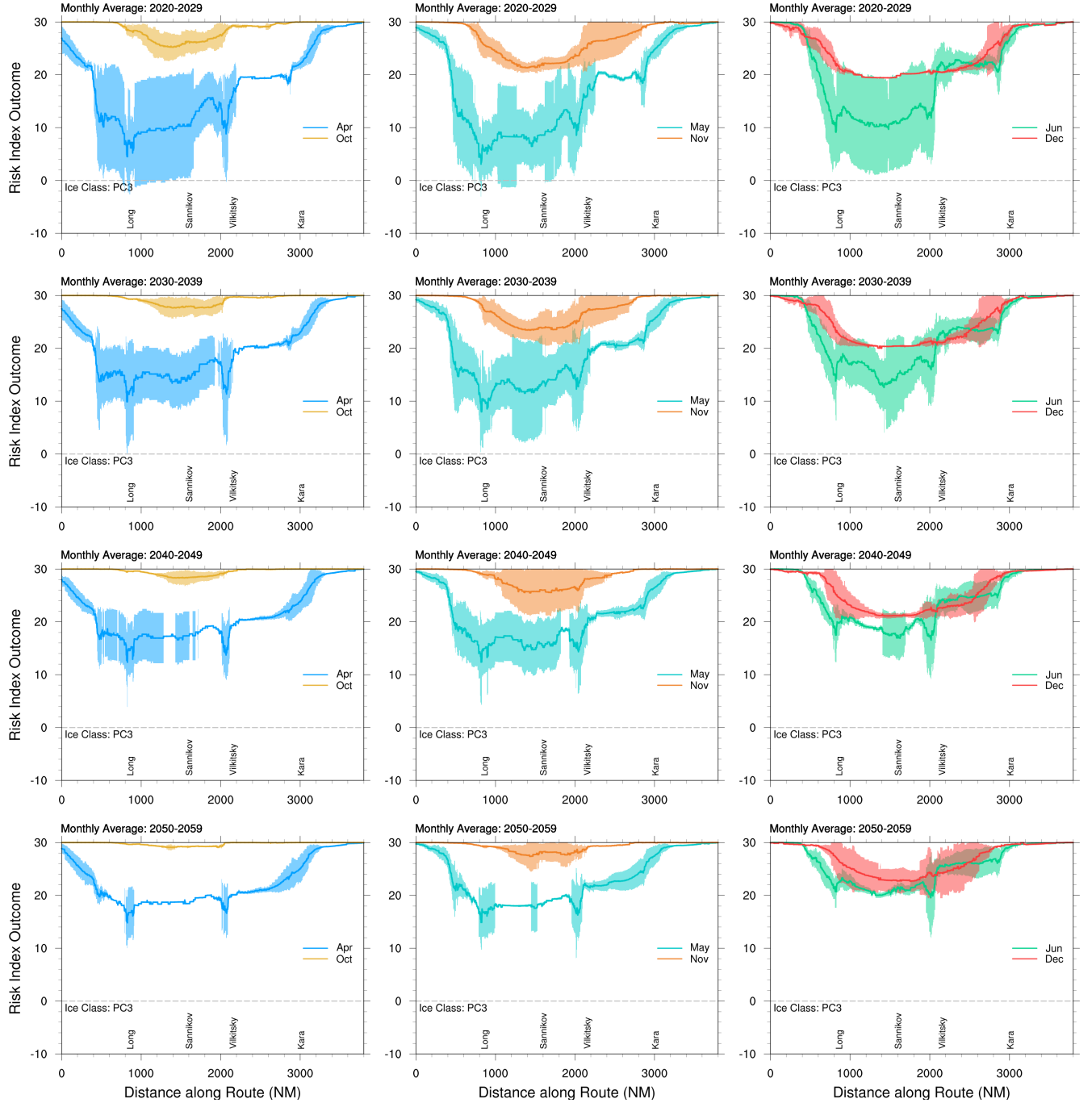


Figure 26: As in Figure 25, but RIOs indicate means and spread along route 20 for different months of the decades 2020–2029 through 2050–2059. The distances of the four straits along the Siberian North coast refer to route 6 and are shown as a reference.